

*Supporting Information for:*

**Bridging Photochemistry and Photomechanics with NMR  
Crystallography: the Molecular Basis for the Macroscopic  
Expansion of an Anthracene Ester Nanorod**

Kevin R. Chalek,<sup>(1)</sup> Xinning Dong,<sup>(1)</sup> Fei Tong,<sup>(1)</sup> Ryan A. Kudla,<sup>(1)</sup> Lingyan Zhu,<sup>(1)</sup> Adam D.  
Gill,<sup>(2)</sup> Chen Yang,<sup>(1)</sup> Alviclér Magalhães,<sup>(3)</sup> Rabih O. Al-Kaysi,<sup>(4)</sup> Joshua D. Hartman,<sup>(1)</sup>  
Wenwen Xu,<sup>(5)</sup> Ryan C. Hayward,<sup>(5)</sup> Richard J. Hooley,<sup>(1)</sup> Gregory J.O. Beran,<sup>(1)</sup>  
Christopher J. Bardeen,<sup>(1)\*</sup> and Leonard J. Mueller<sup>(1)\*</sup>

<sup>(1)</sup> Department of Chemistry  
<sup>(2)</sup> Department of Biochemistry  
University of California, Riverside  
Riverside, CA 92521 (USA)

<sup>(3)</sup> Department of Organic Chemistry  
Institute of Chemistry  
Federal University of Rio de Janeiro  
Rio de Janeiro, RJ, 21941-909  
Brazil

<sup>(4)</sup> College of Science and Health Professions-3124,  
King Saud bin Abdulaziz University for Health Sciences, and King Abdullah International  
Medical Research Center, Ministry of National Guard Health Affairs, Riyadh 11426,  
Kingdom of Saudi Arabia

<sup>(5)</sup> Department of Polymer Science and Engineering  
University of Massachusetts Amherst  
120 Governors Drive  
Amherst, MA 01003

## Table of Contents

<i>Photodimerization reaction of 9TBAE with Carbon Numbering</i> .....	S3
<i>Summary of First-Principles Refined Monomer and Dimer Crystal Structures</i> .....	S4
<i>Summary of First-Principles Chemical Shift and Dipolar Coupling Tensors</i> .....	S5
<i>Flat Coil NMR Probe</i> .....	S11
<i>Experimental Chemical Shift Tensors for <b>9TBAE</b> Monomer</i> .....	S12
<i>Comparison of First-Principles and Experimental Chemical Shift Tensors for the <b>9TBAE</b> Monomer and Dimer</i> .....	S17
<i>Density Matrix Simulations of NMR Spectra</i> .....	S18
<i>Error Surfaces for the Orientation of the Monomer and Dimer Unit Cells</i> .....	S20
<i>Oriented Crystal Solid-State NMR of <sup>13</sup>C15-<b>9TBAE</b></i> .....	S24
<i>Oriented Crystal Solid-State NMR of <sup>13</sup>C<sub>4</sub>-tBu-<b>9TBAE</b> Nanorods at 10% Labeling</i> .....	S26
<i>Linewidth Modeled as a Distribution of Alignment Angles</i> .....	S27
<i>PXRD and GIWAXS Experiments</i> .....	S28
<i>Synthesis of <sup>13</sup>C-Labeled <b>9TBAE</b> Compounds</i> .....	S36
<i>References</i> .....	S48

## Photodimerization reaction of 9TBAE with Carbon Numbering

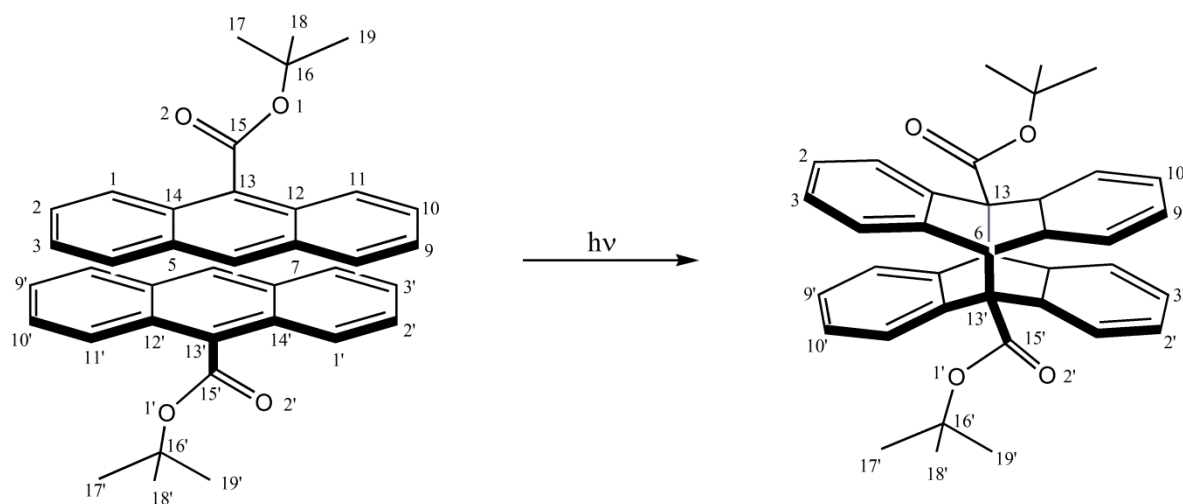


**Figure S1.** The photodimerization reaction of 9-tertbutyl anthracene ester. Select carbon numbering is shown.

## **Summary of First-Principles Refined Monomer and Dimer Crystal Structures**

We have previously reported the solid-state DFT refinement of both the **9TBAE** monomer<sup>1</sup> and SSRD<sup>2</sup>. At room temperature, the electron density for the t-butyl ester group in the monomer shows two unequally populated conformers with relative populations of 0.69 and 0.31; the major conformer is referred to below as conformer A and the minor as conformer B. The refined crystal information files (CIF) are part of the Supporting Information and labeled:

monomer\_struc\_A\_69percent\_1H\_opt.cif

monomer\_struc\_B\_31percent\_1H\_opt.cif

dimer\_pccn\_opt.cif.

## Summary of First-Principles Chemical Shift and Dipolar Coupling Tensors

First-principles chemical shift tensors for both the **9TBAE** monomers<sup>1</sup> and SSRD<sup>2</sup> were previously reported as part of benchmarking and NMR-assisted crystallographic studies. Calculated <sup>13</sup>C chemical shieldings ( $\sigma$ ) were converted to chemical shifts ( $\delta$ ) using the linear rescaling relation<sup>3</sup>

$$\delta[TMS(l, neat)] = -0.9674\sigma_{calc} + 179.5,$$

determined in the benchmarking studies at the same level of theory and basis set used here. The dipolar coupling tensors were calculated directly from the refined molecular coordinates as

$$\mathbf{D} = -\frac{\mu_0}{4\pi} \frac{\gamma_I \gamma_S \hbar}{r^3} \begin{pmatrix} 3x^2/r^2 - 1 & 3xy/r^2 & 3xz/r^2 \\ 3xy/r^2 & 3y^2/r^2 - 1 & 3yz/r^2 \\ 3xz/r^2 & 3yz/r^2 & 3z^2/r^2 - 1 \end{pmatrix}$$

where  $\gamma$  is the gyromagnetic ratio and  $\vec{r} = \vec{r}_S - \vec{r}_I = (x, y, z)$  is the internuclear vector<sup>4</sup>.

Both the chemical shift and dipolar tensor calculations took as input the solid-state DFT refined structures above. The experimental spectra are consistent with fast rotational motion about the ester group O1-C16 bond (Figure S1), so the shift and dipolar tensors are taken to be the fast exchange average over the three equivalent rotameric states.

The first-principles chemical shift and shield tensors are summarized below and are written in the same coordinate frames as the corresponding crystal structures above.

### Monomer:

For the monomer, the electron density for the t-butyl ester group shows two unequally-populated conformers, labeled A and B, with populations of 69% and 31%, respectively; first-principles chemical shifts were calculated independently for each, and the spectroscopic parameters averaged over the two conformations. There are two magnetically inequivalent

asymmetric units in the crystalline unit cell, related by a C2 rotation about the crystallographic *b* (Cartesian *y*) axis. Only one site was calculated directly, with the second site generated via C2(*y*) rotation.

*Quaternary carbon chemical shift (in ppm) for each conformer:*

$$\delta_Q^{1A} = \begin{pmatrix} 78.9 & 35.2 & 23.0 \\ 32.7 & 86.9 & -23.4 \\ 23.29 & -24.8 & 89.2 \end{pmatrix}, \delta_Q^{1B} = \begin{pmatrix} 68.4 & 33.9 & 21.9 \\ 30.4 & 82.7 & -22.4 \\ 20.2 & -24.8 & 87.6 \end{pmatrix}$$

Average chemical shift under fast exchange between major and minor conformer:

$$\delta_Q^1 = 0.69\delta_Q^{1A} + 0.31\delta_Q^{1B}$$

Quaternary carbon chemical shift in magnetically inequivalent asymmetric unit:

$$\delta_Q^2 = C_2(y)\delta_Q^1 C_2^{-1}(y)$$

*Methyl carbon chemical shift (in ppm) for each conformer:*

$$\delta_{Me1}^{1A} = \begin{pmatrix} 40.2 & 8.1 & -5.2 \\ 7.0 & 21.3 & 14.4 \\ -3.2 & 11.2 & 17.9 \end{pmatrix}, \delta_{Me2}^{1A} = \begin{pmatrix} 21.0 & -15.2 & 3.6 \\ -18.6 & 28.9 & 2.3 \\ 6.8 & 1.8 & 48.7 \end{pmatrix}$$

$$\delta_{Me3}^{1A} = \begin{pmatrix} 30.5 & 2.8 & -17.2 \\ 2.0 & 33.7 & -5.9 \\ -20.2 & -4.8 & 12.2 \end{pmatrix}, \delta_{Me1}^{1B} = \begin{pmatrix} 25.5 & 5.7 & -22.4 \\ 5.8 & 34.8 & 0.1 \\ -21.4 & -1.0 & 18.4 \end{pmatrix}$$

$$\delta_{Me2}^{1B} = \begin{pmatrix} 44.4 & -2.8 & 13.4 \\ -7.1 & 32.2 & 13.9 \\ 13.6 & 15.3 & 25.6 \end{pmatrix}, \delta_{Me3}^{1B} = \begin{pmatrix} 26.5 & -9.3 & -6.5 \\ -12.9 & 20.0 & -11.5 \\ -9.5 & -11.5 & 35.7 \end{pmatrix}$$

Average methyl chemical shift under fast t-butyl rotation and exchange between conformers:

$$\delta_{Me1}^1 = \delta_{Me2}^1 = \delta_{Me3}^1 = 0.69(\delta_{Me1}^{1A} + \delta_{Me2}^{1A} + \delta_{Me3}^{1A})/3 + 0.31(\delta_{Me1}^{1B} + \delta_{Me2}^{1B} + \delta_{Me3}^{1B})/3$$

Average methyl carbon chemical shift in magnetically inequivalent asymmetric unit:

$$\delta_{Me}^2 = \mathbf{C}_2(y)\delta_{Me}^1\mathbf{C}_2^{-1}(y)$$

*Dipolar coupling (Hz) for quaternary carbon to each methyl for both conformers:*

$$\mathbf{D}_{Q-Me1}^{1A} = -\begin{pmatrix} -434 & 420 & 1224 \\ 420 & -807 & 797 \\ 1224 & 797 & 1241 \end{pmatrix}, \mathbf{D}_{Q-Me2}^{1A} = -\begin{pmatrix} 1073 & 1452 & -482 \\ 1452 & -101 & -325 \\ -482 & -325 & -972 \end{pmatrix},$$

$$\mathbf{D}_{Q-Me3}^{1A} = -\begin{pmatrix} -936 & -526 & 410 \\ -526 & 846 & -1501 \\ 410 & -1501 & 90 \end{pmatrix}, \mathbf{D}_{Q-Me1}^{1B} = -\begin{pmatrix} -366 & 1212 & 579 \\ 1211 & 976 & 982 \\ 579 & 982 & -610 \end{pmatrix},$$

$$\mathbf{D}_{Q-Me2}^{1B} = -\begin{pmatrix} -501 & 728 & -1005 \\ 728 & -164 & -1264 \\ -1005 & -1264 & 665 \end{pmatrix}, \mathbf{D}_{Q-Me3}^{1B} = -\begin{pmatrix} 426 & -626 & 1490 \\ -626 & -820 & -619 \\ 1490 & -619 & 394 \end{pmatrix}$$

Average dipolar coupling under fast exchange within each conformer and between conformers:

$$\begin{aligned} \mathbf{D}_{Q-MeX}^1 &= \mathbf{D}_{Q-Me1}^1 = \mathbf{D}_{Q-Me2}^1 = \mathbf{D}_{Q-Me3}^1 \\ &= 0.69(\mathbf{D}_{Q-Me1}^{1A} + \mathbf{D}_{Q-Me2}^{1A} + \mathbf{D}_{Q-Me3}^{1A})/3 + 0.31(\mathbf{D}_{Q-Me1}^{1B} + \mathbf{D}_{Q-Me2}^{1B} + \mathbf{D}_{Q-Me3}^{1B})/3 \end{aligned}$$

Average dipolar coupling in magnetically inequivalent asymmetric unit:

$$\mathbf{D}_{Q-MeX}^2 = \mathbf{C}_2(y)\mathbf{D}_{Q-MeX}^1\mathbf{C}_2^{-1}(y)$$

*Dipolar coupling (Hz) between methyl carbons:*

$$\mathbf{D}_{Me1-Me2}^{1A} = \mathbf{D}_{Me2-Me1}^{1A} = -\begin{pmatrix} -142.5 & 208.3 & -123.6 \\ 208.3 & 219.1 & -271.0 \\ -123.6 & -271.0 & -76.7 \end{pmatrix},$$

$$\mathbf{D}_{Me1-Me3}^{1A} = \mathbf{D}_{Me3-Me1}^{1A} = -\begin{pmatrix} 176.2 & 275.5 & 218.4 \\ 275.5 & -54.0 & 145.5 \\ 218.4 & 145.5 & -122.2 \end{pmatrix},$$

$$\mathbf{D}_{Me2-Me3}^{1A} = \mathbf{D}_{Me3-Me2}^{1A} = -\begin{pmatrix} -126.0 & -81.6 & 245.7 \\ -81.6 & -177.8 & -179.7 \\ 245.7 & -179.7 & 303.8 \end{pmatrix},$$

$$\mathbf{D}_{Me1-Me2}^{1B} = \mathbf{D}_{Me2-Me1}^{1B} = - \begin{pmatrix} -220.1 & -55.0 & 95.1 \\ -55.1 & -63.0 & -301.4 \\ 95.1 & -301.4 & 283.1 \end{pmatrix},$$

$$\mathbf{D}_{Me1-Me3}^{1B} = \mathbf{D}_{Me3-Me1}^{1B} = - \begin{pmatrix} -26.2 & 314.4 & -83.9 \\ 314.4 & 230.4 & -124.8 \\ -83.9 & -124.8 & -204.2 \end{pmatrix},$$

$$\mathbf{D}_{Me2-Me3}^{1B} = \mathbf{D}_{Me3-Me2}^{1B} = - \begin{pmatrix} 111.9 & 156.0 & 320.2 \\ 156.0 & -167.9 & 142.9 \\ 320.2 & 142.9 & 55.9 \end{pmatrix}$$

Average methyl-methyl dipolar coupling under fast exchange within each conformer and between conformers:

$$\begin{aligned} \mathbf{D}_{Me-Me}^1 &= \mathbf{D}_{MeA-MeB}^1 = \mathbf{D}_{MeB-MeA}^1 \\ &= 0.69(\mathbf{D}_{Me1-Me2}^{1A} + \mathbf{D}_{Me2-Me3}^{1A} + \mathbf{D}_{Me3-Me1}^{1A})/3 + 0.31(\mathbf{D}_{Me1-Me2}^{1B} + \mathbf{D}_{Me2-Me3}^{1B} + \mathbf{D}_{Me3-Me1}^{1B})/3 \end{aligned}$$

Average dipolar coupling in magnetically inequivalent asymmetric unit:

$$\mathbf{D}_{Me-Me}^2 = \mathbf{C}_2(y) \mathbf{D}_{Me-Me}^1 \mathbf{C}_2^{-1}(y)$$

Carbonyl carbon chemical shift (in ppm) for each conformer:

$$\delta_{CO}^{1A} = \begin{pmatrix} 224.3 & -35.3 & -68.7 \\ -7.4 & 154.2 & 12.8 \\ -61.7 & 26.8 & 145.5 \end{pmatrix}, \quad \delta_{CO}^{1B} = \begin{pmatrix} 187.3 & -33.0 & -67.8 \\ -11.8 & 145.7 & 2.6 \\ -74.0 & 22.5 & 159.7 \end{pmatrix}$$

Average chemical shift under fast exchange between major and minor conformer:

$$\delta_{CO}^1 = 0.69\delta_{CO}^{1A} + 0.31\delta_{CO}^{1B}$$

Quaternary carbon chemical shift in magnetically inequivalent asymmetric unit:

$$\delta_{CO}^2 = \mathbf{C}_2(y) \delta_{CO}^1 \mathbf{C}_2^{-1}(y)$$

### Dimer:

The dimer unit cell has 4 magnetically inequivalent asymmetric units within the unit cell, related by  $C_2$  rotations about the crystallographic  $a$ ,  $b$ , and  $c$  axes (Cartesian  $x$ ,  $y$ , and  $z$  axes, respectively).

Quaternary carbon chemical shift (in ppm):

$$\delta_Q^1 = \begin{pmatrix} 60.0 & -0.8 & 43.6 \\ -1.0 & 111.3 & 0.8 \\ 41.9 & 0.6 & 90.1 \end{pmatrix}$$

Quaternary carbon chemical shift in magnetically inequivalent asymmetric units:

$$\delta_Q^2 = C_2(x)\delta_Q^1 C_2^{-1}(x)$$

$$\delta_Q^3 = C_2(z)\delta_Q^1 C_2^{-1}(z)$$

$$\delta_Q^4 = C_2(y)\delta_Q^1 C_2^{-1}(y)$$

Methyl carbon chemical shift (in ppm):

$$\delta_{Me1}^1 = \begin{pmatrix} 31.0 & -12.7 & 1.5 \\ -10.0 & 7.5 & -9.1 \\ -1.5 & -7.4 & 42.3 \end{pmatrix}, \delta_{Me2}^1 = \begin{pmatrix} 29.8 & 14.2 & -0.4 \\ 11.4 & 11.9 & 10.7 \\ -3.2 & 9.0 & 41.0 \end{pmatrix}$$

$$\delta_{Me3}^1 = \begin{pmatrix} 35.4 & -0.6 & -10.2 \\ -1.1 & 48.7 & -2.3 \\ -9.6 & -2.5 & 7.7 \end{pmatrix}$$

Average methyl chemical shift under fast t-butyl rotation:

$$\delta_{Me}^1 = (\delta_{Me1}^1 + \delta_{Me2}^1 + \delta_{Me3}^1) / 3$$

Average methyl carbon chemical shift in magnetically inequivalent asymmetric units:

$$\delta_{Me}^2 = C_2(x)\delta_{Me}^1 C_2^{-1}(x)$$

$$\delta_{Me}^3 = C_2(z)\delta_{Me}^1 C_2^{-1}(z)$$

$$\delta_{Me}^4 = \mathbf{C}_2(y) \delta_{Me}^1 \mathbf{C}_2^{-1}(y)$$

Dipolar coupling (Hz) for quaternary carbon to each methyl:

$$\mathbf{D}_{Q-Me1}^1 = - \begin{pmatrix} -784 & 46 & 932 \\ 46 & -1073 & 144 \\ 932 & 144 & 1857 \end{pmatrix}, \quad \mathbf{D}_{Q-Me2}^1 = - \begin{pmatrix} -108 & -1422 & 428 \\ -1422 & 999 & -627 \\ 428 & -627 & -891 \end{pmatrix},$$

$$\mathbf{D}_{Q-Me3}^1 = - \begin{pmatrix} -327 & 1339 & 283 \\ 1339 & 1301 & 503 \\ 283 & 503 & -974 \end{pmatrix}$$

Average dipolar coupling under fast t-butyl rotation:

$$\mathbf{D}_{Q-MeX}^1 = (\mathbf{D}_{Q-Me1}^1 + \mathbf{D}_{Q-Me2}^1 + \mathbf{D}_{Q-Me3}^1) / 3$$

Average dipolar coupling in magnetically inequivalent asymmetric units:

$$\mathbf{D}_{Q-MeX}^2 = \mathbf{C}_2(x) \mathbf{D}_{Q-MeX}^1 \mathbf{C}_2^{-1}(x)$$

$$\mathbf{D}_{Q-MeX}^3 = \mathbf{C}_2(z) \mathbf{D}_{Q-MeX}^1 \mathbf{C}_2^{-1}(z)$$

$$\mathbf{D}_{Q-MeX}^4 = \mathbf{C}_2(y) \mathbf{D}_{Q-MeX}^1 \mathbf{C}_2^{-1}(y)$$

Carbonyl carbon chemical shift (in ppm):

$$\delta_{CO}^1 = \begin{pmatrix} 177.6 & -1.3 & -33.6 \\ -2.2 & 112.1 & 3.8 \\ -66.6 & 3.5 & 239.5 \end{pmatrix}$$

Carbonyl carbon chemical shift in magnetically inequivalent asymmetric units:

$$\delta_{CO}^2 = \mathbf{C}_2(x) \delta_{CO}^1 \mathbf{C}_2^{-1}(x)$$

$$\delta_{CO}^3 = \mathbf{C}_2(z) \delta_{CO}^1 \mathbf{C}_2^{-1}(z)$$

$$\delta_{CO}^4 = \mathbf{C}_2(y) \delta_{CO}^1 \mathbf{C}_2^{-1}(y)$$

## Flat Coil NMR Probe

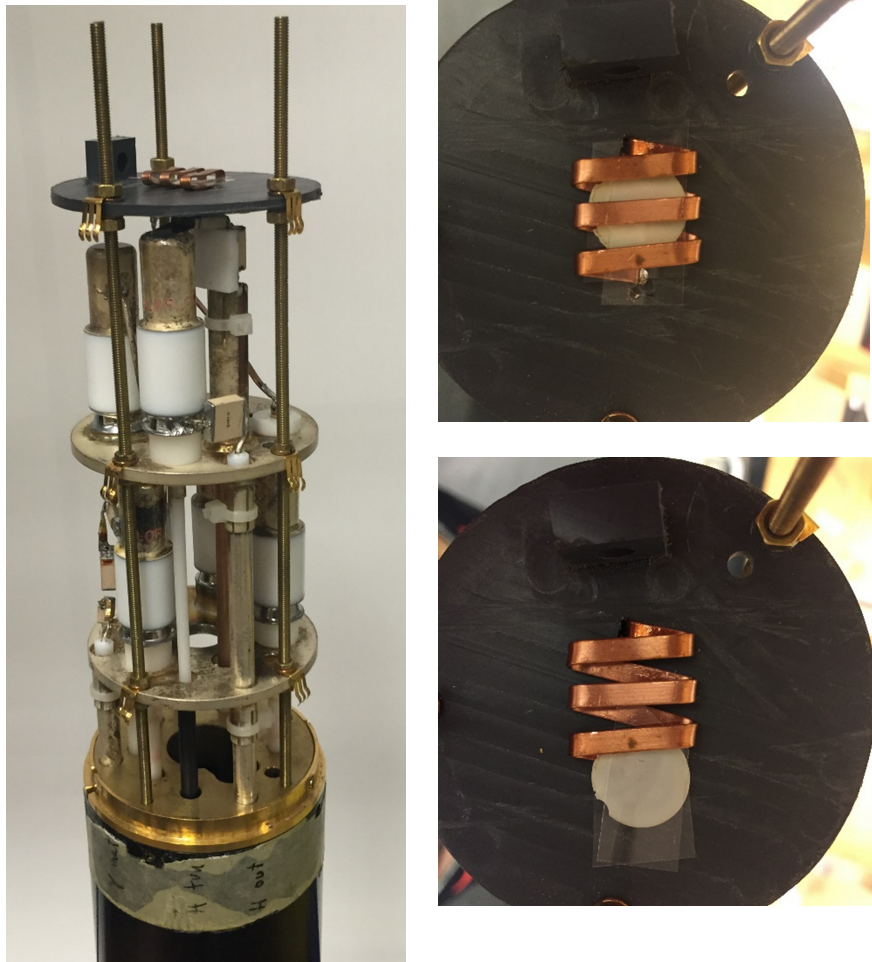


**Figure S2:** Flat coil NMR probe (left) and close-up of the AAO template containing oriented 9TBAE nanorods (right) being inserted into the flat coil.

## **Experimental Chemical Shift Tensors for the 9TBAE Monomer**

**Chemical Shift Tensors:** Experimental chemical shift tensors were measured using a combination of the TOSS-t<sub>1</sub>-deTOSS approach of Kolbert and Griffin<sup>5</sup> and the extended CSA amplification (xCSA) method of Hung and Gan<sup>6</sup>, both modified as previously described<sup>2</sup>. TOSS-t<sub>1</sub>-deTOSS experiments were performed at 14.1 T (600.01 MHz <sup>1</sup>H, 150.87 MHz <sup>13</sup>C) on a Bruker AVANCE I spectrometer equipped with a 4 mm double resonance MAS probe with samples spinning at 2 kHz; cross-polarization was implemented using spin lock fields 38 kHz on <sup>13</sup>C and a ramped field of 36-40 kHz on <sup>1</sup>H with a 2 ms contact time; other RF powers were 83 kHz <sup>1</sup>H (excitation and decoupling) and 50 kHz <sup>13</sup>C ( $\pi$  and  $\pi/2$  pulses). xCSA experiments were performed at 9.4 T (400.37 MHz <sup>1</sup>H, 100.68 MHz <sup>13</sup>C) on a Bruker AVANCE III spectrometer equipped with a 4 mm double resonance MAS probe with samples spinning at 3.125 kHz; cross-polarization spin lock fields were 41 kHz on <sup>13</sup>C and 36–42 kHz (linearly ramped) on <sup>1</sup>H, with a 2 ms contact time; other RF powers were 83 kHz <sup>1</sup>H (excitation and decoupling) and 50 kHz <sup>13</sup>C ( $\pi$  and  $\pi/2$  pulses). <sup>13</sup>C chemical shifts were referenced indirectly to neat TMS via an external solid-state sample of adamantane with the downfield-shifted peak set to 38.48 ppm<sup>7</sup>. Tensor components were determined by a fit of the sideband intensities using Herzfeld-Berger analysis<sup>8</sup> within Bruker BioSpin's *Topspin 3.0* processing software and are summarized in Table S1. For xCSA experiments, the summed center band (isotropic) and sideband traces were summed before Herzfeld-Berger analysis.

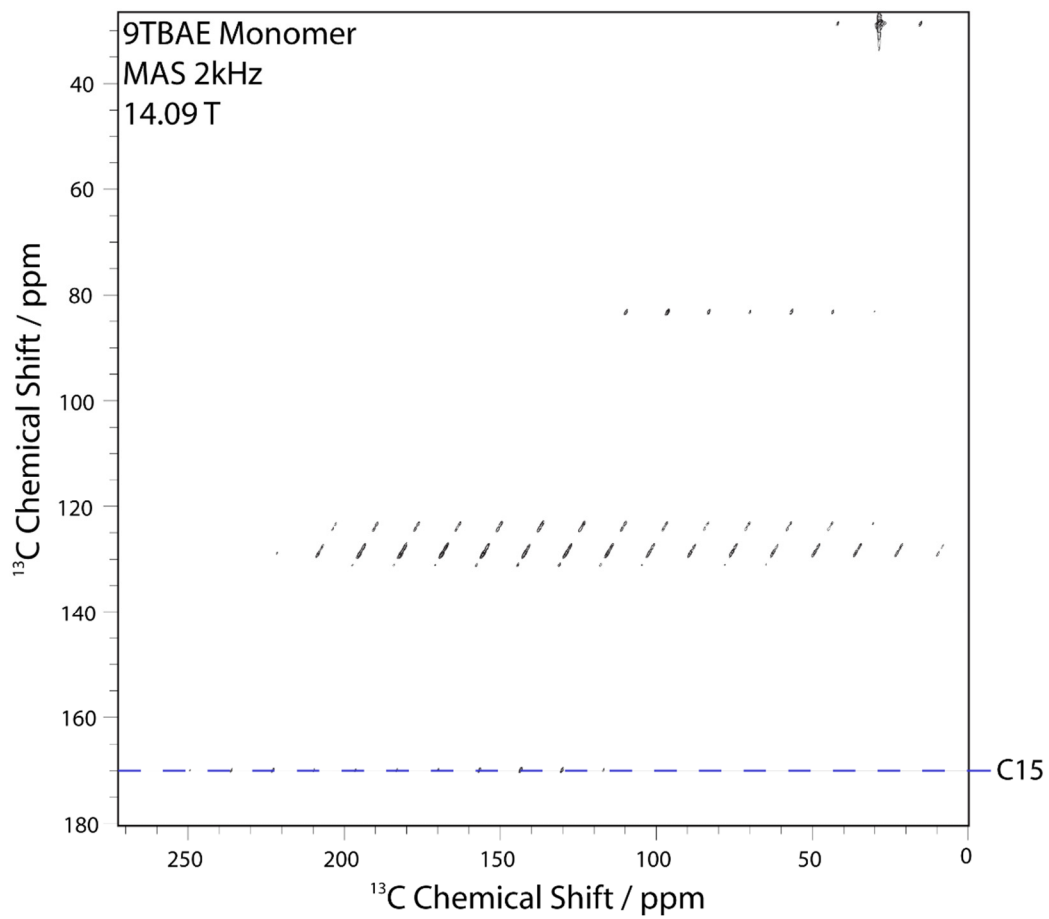


**Figure S3:** The TOSS-deTOSS of the monomeric **9TBAE** at 14.09 T and 2kHz MAS.

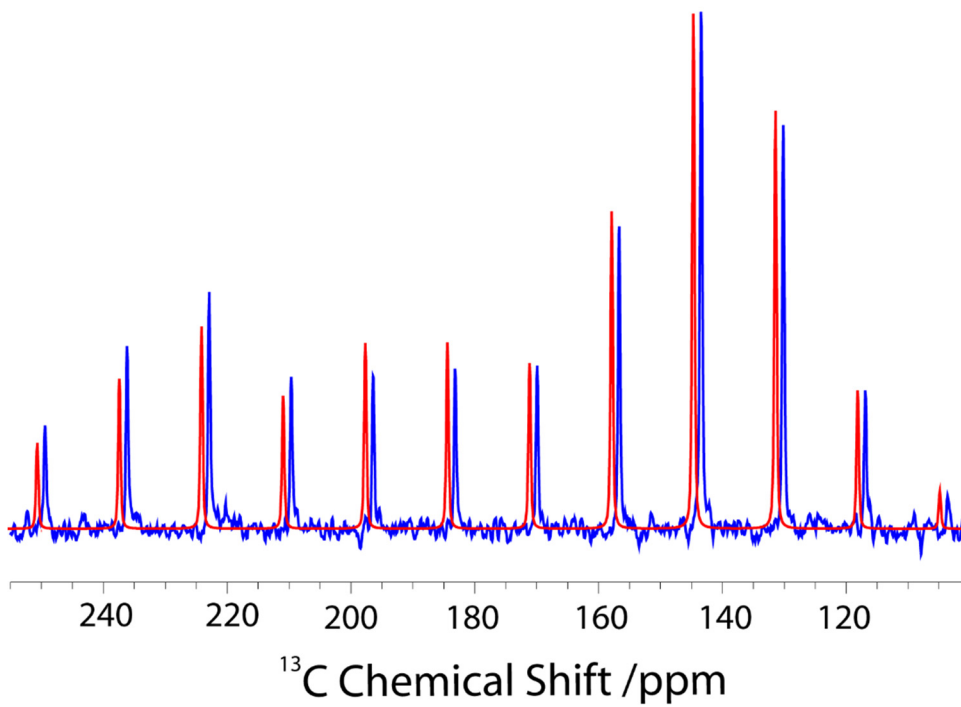


**Figure S4:** 1D trace (blue) from the monomer TOSS-deTOSS spectrum used for extracting the CSA tensors via Herzfeld-Berger analysis (red) for C15.

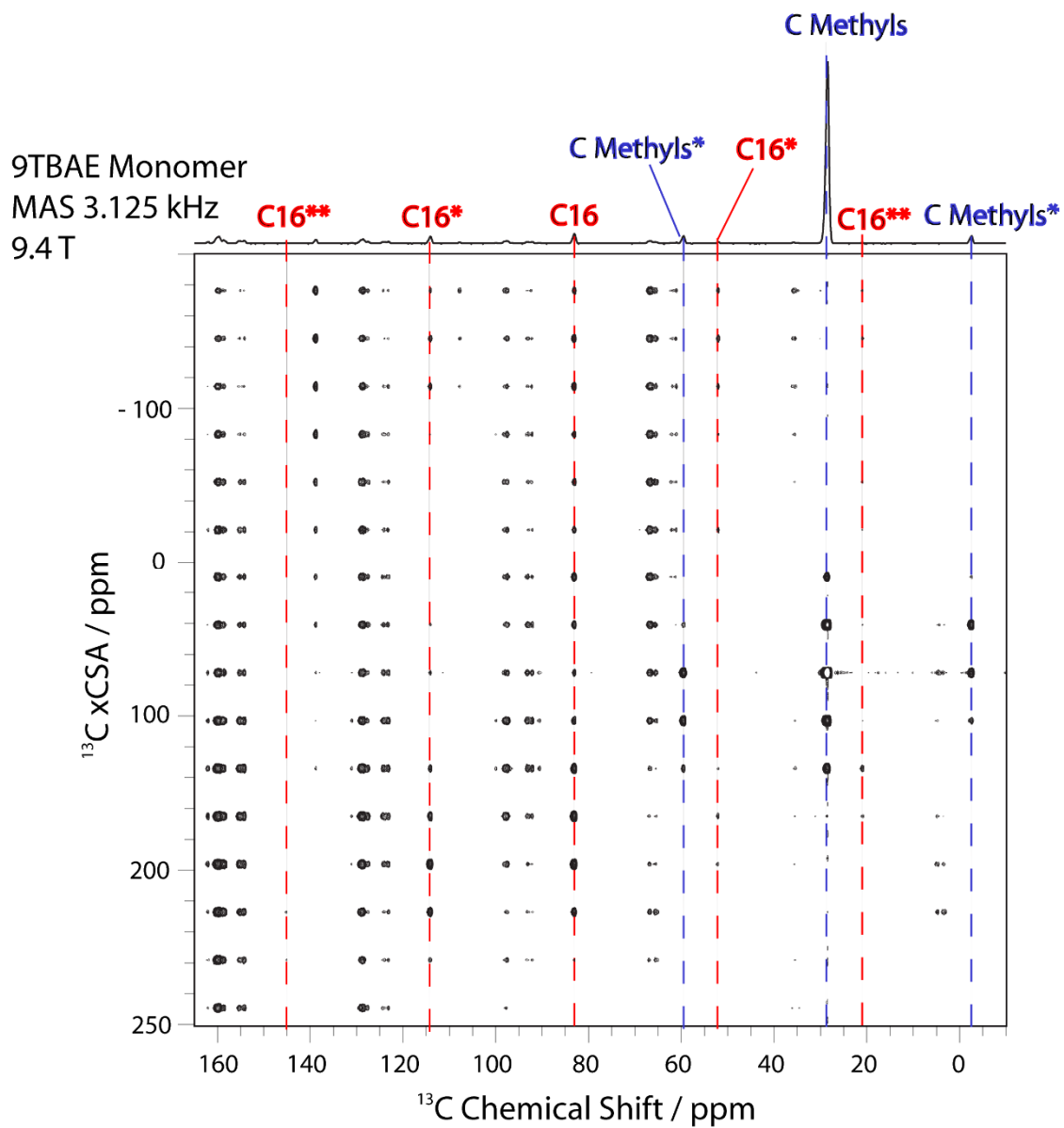
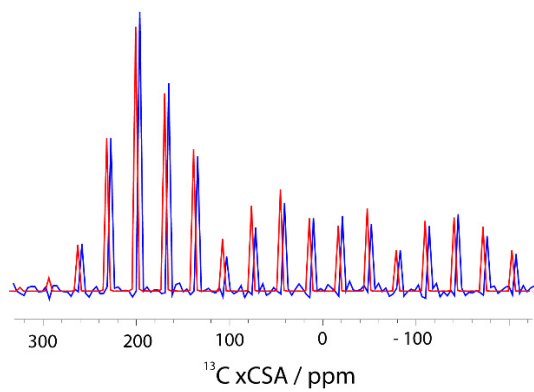


**Figure S5:** The xCSA spectrum of the monomer at 9.4 T and 3.125 kHz MAS. Center band (isotropic) and sideband traces used in the CSA analysis are indicated.

C16



C17-19

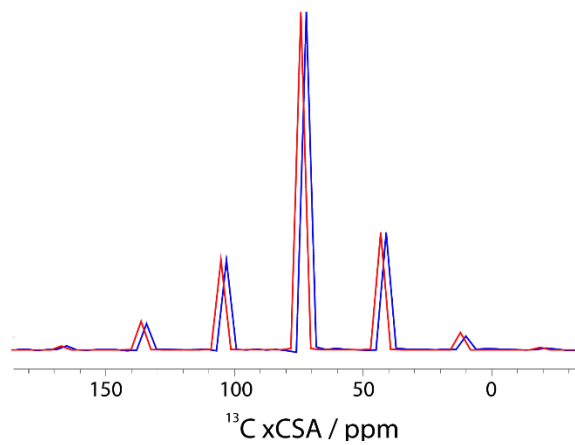


**Figure S6:** Summed center and sideband 1D traces (blue) from the monomer xCSA spectrum used for extracting the CSA tensors via Herzfeld-Berger analysis (red) for the indicated carbon sites.



## Density Matrix Simulations of NMR Spectra

Four-spin NMR simulations were carried out in the Mathematica™ programming environment using a numerical density matrix approach in the simple product basis. Beginning with an initial density matrix corresponding to x-magnetization,

$$\rho(0) = I_{Q,X} + I_{Me1,X} + I_{Me2,X} + I_{Me3,X},$$

the time-dependent density matrix was calculated by direct matrix exponentiation and multiplication

$$\rho(t) = \exp(-i\mathbf{H}t)\rho(0)\exp(i\mathbf{H}t).$$

The time-domain signal was calculated as the trace of the density matrix with  $\mathbf{I}_+$

$$s(t) = \text{Tr}\{\rho(t)\mathbf{I}_+\}$$

and the frequency-domain spectrum generated by Fourier transformation of this signal.

The fast-exchange Hamiltonian (in rad/s) for the four-spin coupled system was composed as,

$$\begin{aligned} \mathbf{H} = & \left[ \delta_Q \right]_{ZZ} I_{Q,Z} + \left[ \delta_{Me} \right]_{ZZ} (I_{Me1,Z} + I_{Me2,Z} + I_{Me3,Z}) \\ & + \left[ \mathbf{D}_{Q-Me} \right]_{ZZ} (3I_{Q,Z}I_{Me1,Z} - \mathbf{I}_Q \cdot \mathbf{I}_{Me1} + 3I_{Q,Z}I_{Me2,Z} - \mathbf{I}_{Q2} \cdot \mathbf{I}_{Me2} + 3I_{Q,Z}I_{Me3,Z} - \mathbf{I}_Q \cdot \mathbf{I}_{Me3}) / 2 \\ & + \left[ \mathbf{D}_{Me-Me} \right]_{ZZ} (3I_{Me1,Z}I_{Me2,Z} - \mathbf{I}_{Me1} \cdot \mathbf{I}_{Me2} + 3I_{Me1,Z}I_{Me3,Z} - \mathbf{I}_{Me1} \cdot \mathbf{I}_{Me3} + 3I_{Me2,Z}I_{Me3,Z} - \mathbf{I}_{Me2} \cdot \mathbf{I}_{Me3}) / 2 \\ & + J_{Q-Me} (\mathbf{I}_Q \cdot \mathbf{I}_{Me1} + \mathbf{I}_{Q2} \cdot \mathbf{I}_{Me2} + \mathbf{I}_Q \cdot \mathbf{I}_{Me3}) \end{aligned}$$

Separate simulations were performed for each of the magnetically inequivalent sites. The scalar coupling between the quaternary carbon and the methyl carbons,  $J_{Q-Me}$ , was approximated as +35 Hz, and terms  $[\mathbf{A}]_{ZZ}$  indicate the laboratory frame ZZ component of the corresponding spatial tensor. All spatial tensors were initially written in the crystal frame (the tensors given above) and were rotated (with the crystal unit cell) to a final orientation in the laboratory (nanorod) frame using the active rotation convention<sup>9</sup>:

$$\mathbf{A}_{lab} = \mathbf{R}_A(\alpha, \beta, \gamma) \mathbf{A}_{xtal} \mathbf{R}_A^{-1}(\alpha, \beta, \gamma)$$

in which

$$\mathbf{R}_A(\alpha, \beta, \gamma) = \begin{pmatrix} \cos \alpha \cos \beta \cos \gamma - \sin \alpha \sin \gamma & -\cos \alpha \cos \beta \sin \gamma - \sin \alpha \cos \gamma & \cos \alpha \sin \beta \\ \sin \alpha \cos \beta \cos \gamma + \cos \alpha \sin \gamma & -\sin \alpha \cos \beta \sin \gamma + \cos \alpha \cos \gamma & \sin \alpha \sin \beta \\ -\sin \beta \cos \gamma & \sin \beta \sin \gamma & \cos \beta \end{pmatrix}.$$

## Error Surfaces for the Orientation of the Monomer and Dimer Unit Cells

### *Monomer:*

To align the unit cell with respect to the magnetic field, a target spectrum was first constructed that consisted of a best-fit Lorentzian line to the quaternary carbon resonance at 80.1 ppm. Next, the predicted spectrum for a given orientation was modeled as the sum of two equal intensity 1:3:3:1 multiplets – one for each of the two potentially magnetically inequivalent asymmetric units – with frequencies determined by the  $zz$ -components of the chemical shift and dipolar tensors. The Euler angles  $\beta$  and  $\gamma$  (using an active rotation convention<sup>9</sup>) that orient the unit cell in the nanorod/magnetic field frame were then scanned for best agreement with the target spectrum, with the overall spectral intensity and linewidths optimized at each orientation. Note that the spectrum is invariant to the “ $\alpha$ ” Euler angle, which corresponds to a final rotation about the magnetic field axis that does not affect the NMR observables. The error surface (residuals squared) for this scan is shown above and two distinct solution sets (demarked in red and blue) are found and labeled on the surface. Each set consists of several symmetry related/equivalent solutions – two of which derive from the symmetry of the crystalline space group (the rotational

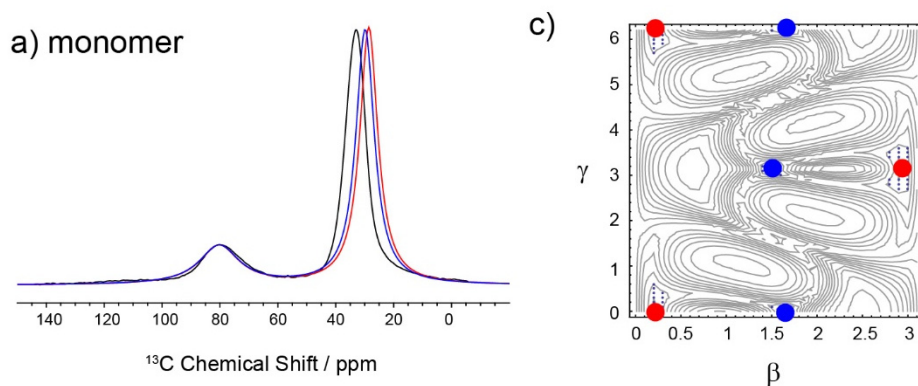


**Figure S7:**  $^{13}\text{C}$  solid-state NMR spectra of ensemble-oriented monomeric  $^{13}\text{C}_4\text{-tBu-9TBAE}$  nanorods within an AAO template with the long rod axes parallel to the magnetic field direction compared to the two (sets of symmetry related) best-fit orientations indicated on the error surface on the right.

component of the S2 screw axis along the crystallographic “b” axis that exchanges the magnetically inequivalent asymmetric units) and a second doubling of solutions due to invariance of the spectral frequencies under a final C2 rotation perpendicular to the lab frame magnetic field. The latter reflects the fact that the NMR spectrum is identical whether the crystal is oriented up or down in the field.

The blue set of solutions correspond to an 84.4° rotation of the unit cell along the crystallographic *-b* axis  $\{\beta=84.4^\circ, \gamma=180^\circ\}$ , placing the (13 0 -1) Miller plane perpendicular to the rod axis (*i.e.*, the (13 0 -1) direction in reciprocal space is normal to the template surface and parallel to the rod axis). For reference, this orientation is 5.6° off the real space [1 0 0] axis and 4° off of the reciprocal space (1 0 0) axis. Therefore, the (1 0 0) Miller plane is nearly perpendicular to the laboratory and nanorod z-axis; the symmetry-related solution  $\{\beta=95.6^\circ, \gamma=0^\circ\}$  rotates the crystal 180° about the unit cell b axis (which is coincident with the laboratory frame y-axis), flipping the (100) plane 180° while maintaining its orthogonal orientation with respect to the nanorod axis. The red set of solutions corresponds to a 10.6° rotation of the unit cell along the crystallographic b axis  $\{\beta=10.6^\circ, \gamma=0^\circ\}$ , nearly aligning the crystallographic c axis, [0 0 1], with the laboratory z-axis; the symmetry-related solution  $\{\beta=169.4^\circ, \gamma=180^\circ\}$  orients [0 0 1] to the laboratory *-z* direction. There are no obvious low order Miller planes for the [0 0 1] family of solutions. Both the (1 0 0) and [0 0 1] sets of solutions reproduce the spectral region of the quaternary carbons equally well, but predict different resonance frequencies for the methyl groups due to their distinct alignments with respect to the laboratory frame magnetic field. The predicted spectra are shown above in the corresponding colors, and the methyl region can be used to distinguish the two sets, showing better agreement with the (1 0 0) family of solutions (predicted shift 29.9 ppm, experimental shift 33.4 ppm). Although the [0 0 1] family of solutions predicts a

methyl shift that is also in reasonable agreement with the experimental value (predicted shift 28.6 ppm), given the expected accuracy with which chemical shifts can be predicted (1.4 ppm RMSE), the (1 0 0) is solution is preferred. Still, the similarities of these two solutions motivated the incorporation of an additional label at the ester carbonyl group that can clearly distinguish the two solutions as shown in the following section.

### *SSRD*

The orientation of the dimer was solved in an analogous fashion to that of the monomer, using a target spectrum that consisted of a best-fit Lorentzian line to the quaternary carbon resonance at 97.3 ppm. For the dimer, the blue set of solutions correspond to a 35.5° rotation of the unit cell along the crystallographic “a” axis  $\{\beta=35.5^\circ, \gamma=90.0^\circ\}$ , nearly placing (within 2°) the [0 1 1] real space axis normal to the surface; the nearest low index Miller plane is (0 1 2), with a reciprocal space normal 2.3° off this axis (but in the opposite direction from [0 1 1]). The symmetry related solutions fall at  $\{\beta=35.5^\circ, \gamma=270.0^\circ\}$ ,  $\{\beta=144.5^\circ, \gamma=90.0^\circ\}$ , and  $\{\beta=144.5^\circ, \gamma=270.0^\circ\}$ , corresponding to real space axes//planes [0 -1 1]//(0 -1 2), [0 1 -1]//(0 1 -2), and [0 -1 -1]//(0 -1 -2) respectively. The red set of solutions fall at  $\{\beta=90^\circ, \gamma=57.9^\circ\}$ ,  $\{\beta=90^\circ, \gamma=121.5^\circ\}$ ,  $\{\beta=90^\circ, \gamma=238.5^\circ\}$ , and  $\{\beta=90^\circ, \gamma=301.5^\circ\}$ , and correspond to the <3 4 0> family of Miller planes being perpendicular to the nanorod axis. The predicted spectra for these two sets of solutions shown in the corresponding colors again show equally good agreement for the quaternary carbons, but the <0 1 2> family of solutions (blue) shows substantially better agreement in the methyl region compared to the <3 4 0> set, 27.5 ppm vs 25.2 ppm, respectively, compared to an experimental value of 30.6 ppm.

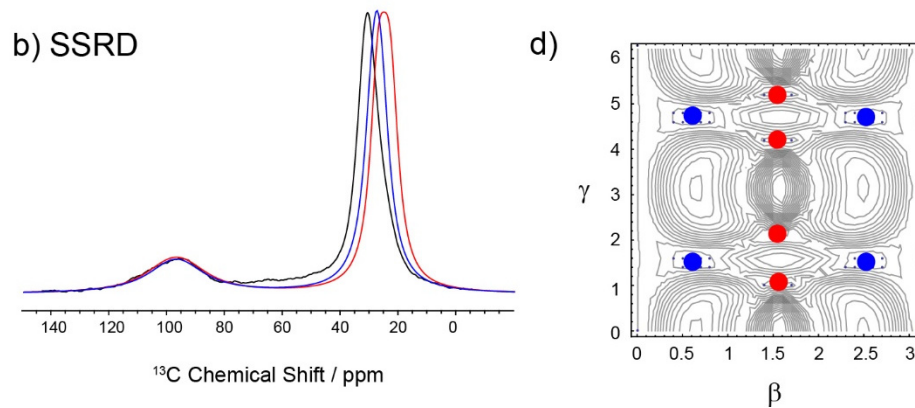


**Figure S8:**  $^{13}\text{C}$  solid-state NMR spectra of ensemble-oriented  $^{13}\text{C}_4\text{-tBu-9TBAE}$  SSRD nanorods within an AAO template with the long rod axes parallel to the magnetic field direction compared to the two (sets of symmetry related) best-fit orientations indicated on the error surface on the right.

## **Oriented Crystal Solid-State NMR of $^{13}\text{C}_{15}\text{-9TBAE}$ to Rule Out Alternate Solutions**

The fine difference between the spectra for the two monomer solutions motivated the incorporation of an additional label at the ester carbonyl group to more clearly distinguish between them. Shown below in black is the  $^{13}\text{C}$  solid-state NMR spectrum of aligned  $^{13}\text{C}_{15}\text{-9TBAE}$  nanorods within an AAO template with the long rod axes parallel to the magnetic field; the carbonyl peak falls at 213 ppm. Shown in blue is the predicted spectrum based on the best-fit orientation corresponding to the (1 0 0) family of solutions for the  $^{13}\text{C}_4\text{-tBu-9TBAE}$  nanorods; in red is the predicted spectrum for the alternate [0 0 1] family of solutions. Note that there are no adjustable parameters in these predicted spectra, making them a sensitive test for the two models. The blue (100) solution (centered at 199 ppm) falls within the expected agreement of (9.2 ppm RMSE) for  $\text{sp}^2$  carbons bound to oxygen, while the red [0 0 1] solution at 175 ppm does not. The red [0 0 1] solutions can therefore be rejected.

A similar analysis for the SSRD shows the experimental peak for the ester carbonyl of the aligned nanorods at 199 ppm (black spectrum) is predicted within expected accuracy by the [0 1 1]//[0 1 2) family of solutions, which give a predicted carbonyl resonance of 196 ppm for this orientation (blue spectrum). In contrast, the <3 4 0> family of Miller planes correspond to a predicted resonance at 130 ppm (red spectrum). Again, it is stressed that there are no adjustable parameters in these predictions. The red <3 4 0> orientation is inconsistent with the additional experimental data for the carbonyl label and can therefore be ruled out.

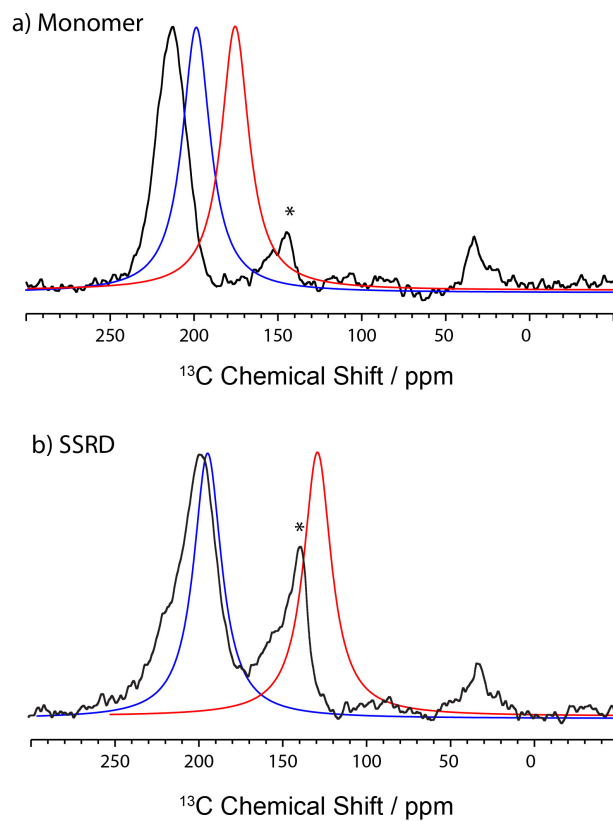


**Figure S9:**  $^{13}\text{C}$  solid-state NMR spectra of ensemble-oriented  $^{13}\text{C}15$ -9TBAE monomer (top) and SSRD (bottom) nanorods within an AAO template with the long rod axes parallel to the magnetic field direction. These are compared to the two best-fit orientations indicated on the error surfaces in Figures S7 and S8 respectively. In both spectra the asterisk marks an impurity that we found difficult to remove from the carbonyl-labeled samples.

Oriented Crystal Solid-State NMR of  $^{13}\text{C}_4\text{-tBu-9TBAE}$  Nanorods at 10% Labeling

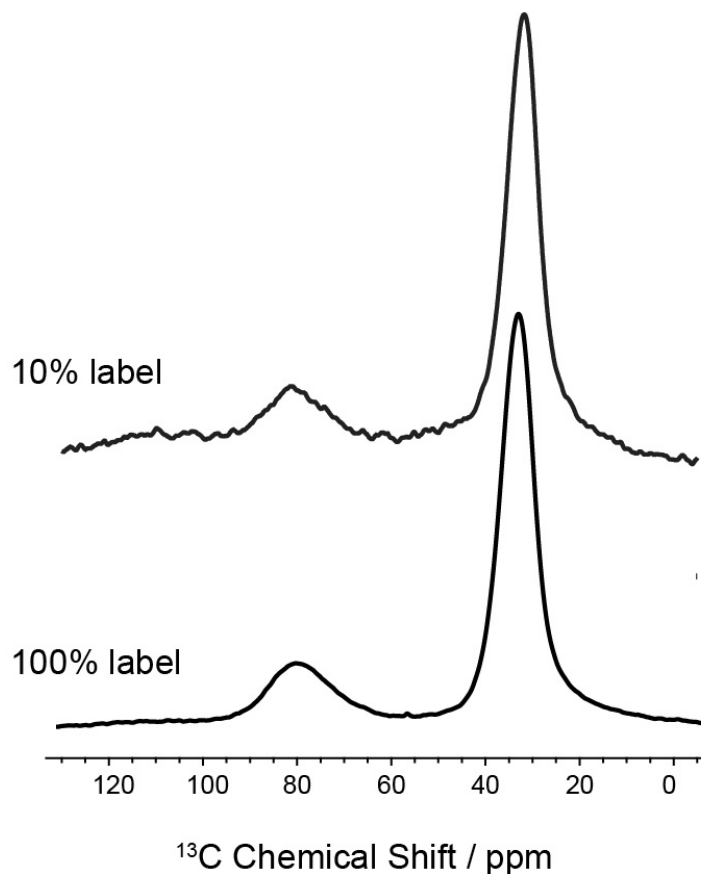


**Figure S10:**  $^{13}\text{C}$  solid-state NMR spectra of ensemble-oriented **9TBAE** nanorods within an AAO template with the long rod axes parallel to the magnetic field direction for samples composed of 100%  $^{13}\text{C}_4\text{-tBu-9TBAE}$  (bottom) and 10%  $^{13}\text{C}_4\text{-tBu-9TBAE}$  (top). The latter nanorods were prepared from a solution composed of 10% of the uniformly labeled **9TBAE** with 90% natural abundance **9TBAE**.

## Linewidth Modeled as a Distribution of Alignment Angles

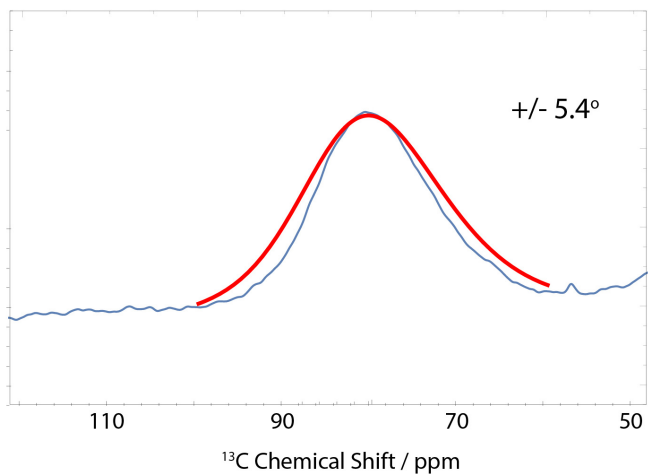
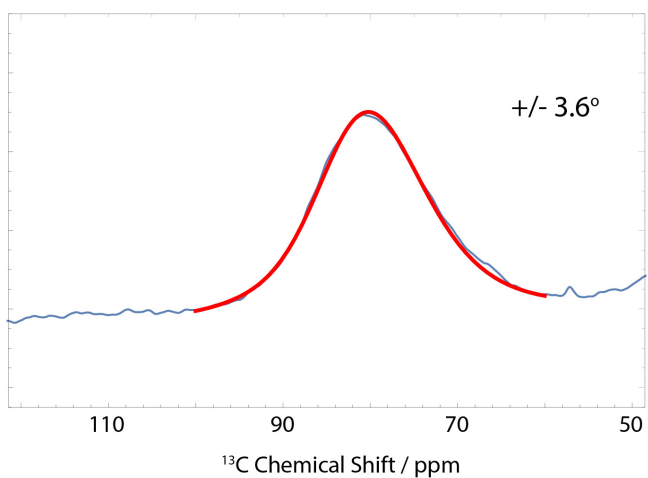
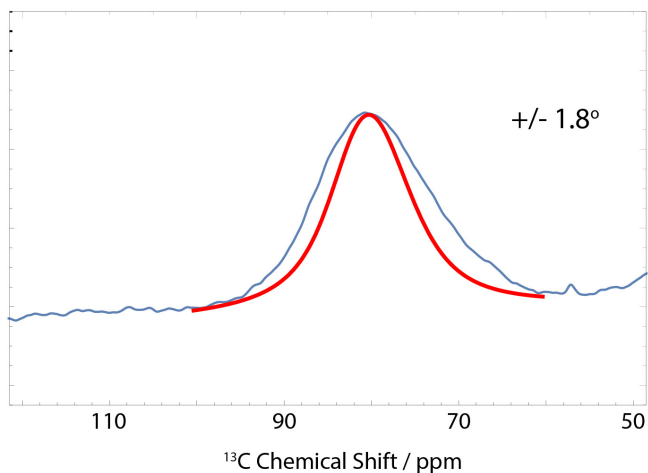


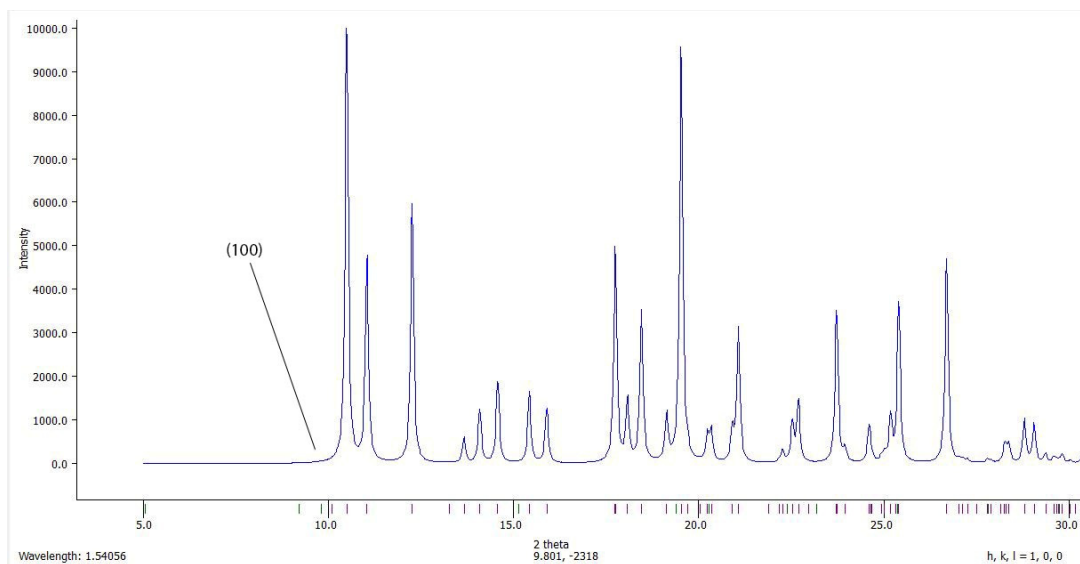
**Figure S11:** Predicted NMR line shapes (red) for the monomer nanorods assuming a Gaussian distribution of alignment angles centered on the best-fit orientation determined above, with a linewidth of 3 ppm (equivalent to the adamantane linewidth) and varying standard deviations indicated for both the  $\beta$  and  $\gamma$  Euler angles. Both the width and asymmetric line shape of the experimental data (blue) are reproduced.

## **Powder XRD and GIWAXS:**

### *PXRD:*

In previous work, we tried to identify the nanorod orientations in the oriented AAO templates using PXRD on 9TBAE nanorods aligned within an AAO template lying horizontally on the diffractometer. In this arrangement, the diffraction intensity is dominated by lines corresponding to Miller planes parallel to the template (perpendicular to the rod axis). This approach tentatively identified peaks corresponding to the (0 1 1) and (1 1 1) Miller planes for the monomer and SSRD in the PXRD data and assumed that these planes were normal to the nanorod axis.<sup>2</sup> However, when we tried to use this monomer crystal orientation to calculate the length change, a contraction of 2.3% in length was predicted, the opposite trend for what was experimentally observed. Based on the new orientations derived from SSNMR, the monomer (1 0 0) and dimer (0 1 -2) Miller planes are approximately normal to the nanorod axis and thus would be expected to appear in the PXRD pattern using the standard Bragg-Brentano geometry. However, numerical simulations performed in the program Mercury (Cambridge Crystallographic Data Centre)<sup>10</sup> predict extremely weak reflection for these particular Miller planes, presumably due to low electron density (Figure S12). As a result, the PXRD patterns were likely dominated by scattering from surface debris and did not reflect the orientation of the nanorods underneath.

## Monomer:



## Dimer:

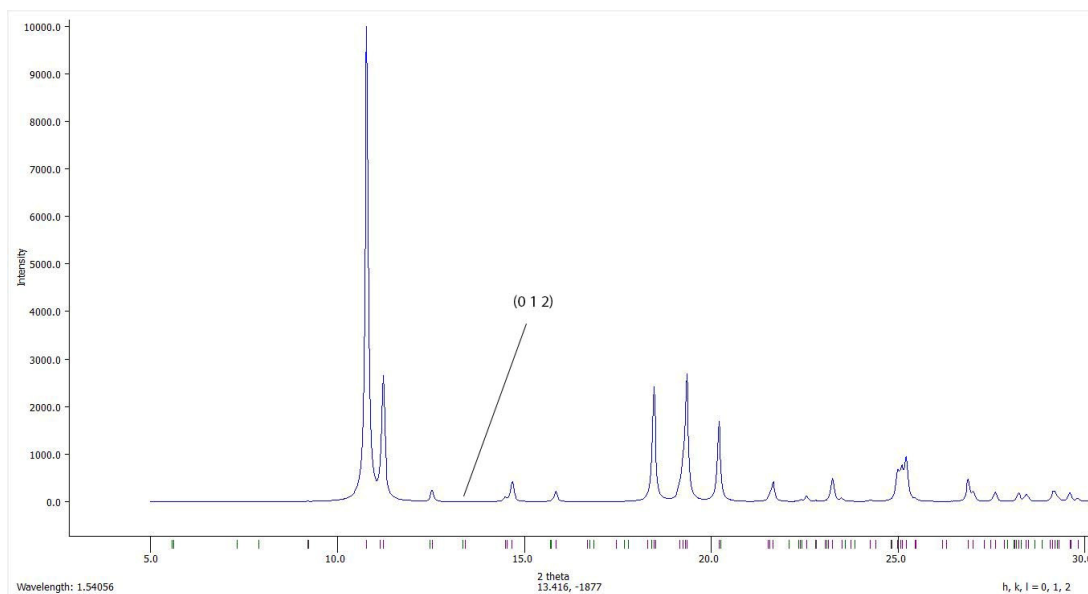


**Figure S12:** Numerical simulations of the PXRD spectra performed in Cambridge Crystallographic Data Centre's Mercury CSD viewer<sup>10</sup> predict extremely weak reflection from the monomer (100) and dimer (012) Miller planes, presumably due to low electron density for those planes.

## GIWAXS:

To confirm the crystal orientations deduced from the SSNMR, GIWAXS measurements were undertaken on the oriented AAO templates. The GIWAXS experiment acquires diffraction information across a range of angles, so it is sensitive to crystal planes with different orientations with respect to the surface plane. Figure S13a shows the diffraction pattern for the monomer-filled template. The 011 and 002 reflections are both along the film plane direction (indicated by a white line), suggesting that the [1 0 0] direction in real space is closely aligned with the surface normal. Further confirmation of this assignment is provided by the excellent match between the expected positions of each of the other diffraction spots (calculations are described in detail in the Supporting Information) and the experimental data (Table S3). This orientation agrees to within  $5.6^\circ$  with the orientation from SSNMR. Upon UV exposure (365 nm, 20 mW/cm<sup>2</sup>, 6 h), the monomer crystal is transformed into the dimer crystal, as witnessed by the disappearance of monomer reflections and the appearance of strong dimer reflections in Figure 6b. The **9TBAE** dimer diffraction pattern is indexed based on the SSRD crystal structure published previously.<sup>2</sup> Since the 111 and 122 reflections are both in-plane, the dimer surface normal direction is assigned to be [0 1 -1] in real space. Once again, the GIWAXS results show a good match with SSNMR, with absolute alignments differing by only  $2^\circ$ . This assignment of the orientation also leads to a match between the measured and expected locations of all other observed dimer diffraction peaks (Table S4). We note that the dimer GIWAXS pattern contains a diffraction spot at  $q = 1.4 \text{ \AA}^{-1}$  that can be assigned to unreacted monomer.<sup>11</sup> The average FWHM of scattering peaks along the azimuthal direction in the samples is  $3.7^\circ$  for the monomer (Figure S14) and  $5.4^\circ$  for the dimer (Figure S15), suggesting a high degree of alignment with respect to the film normal direction.

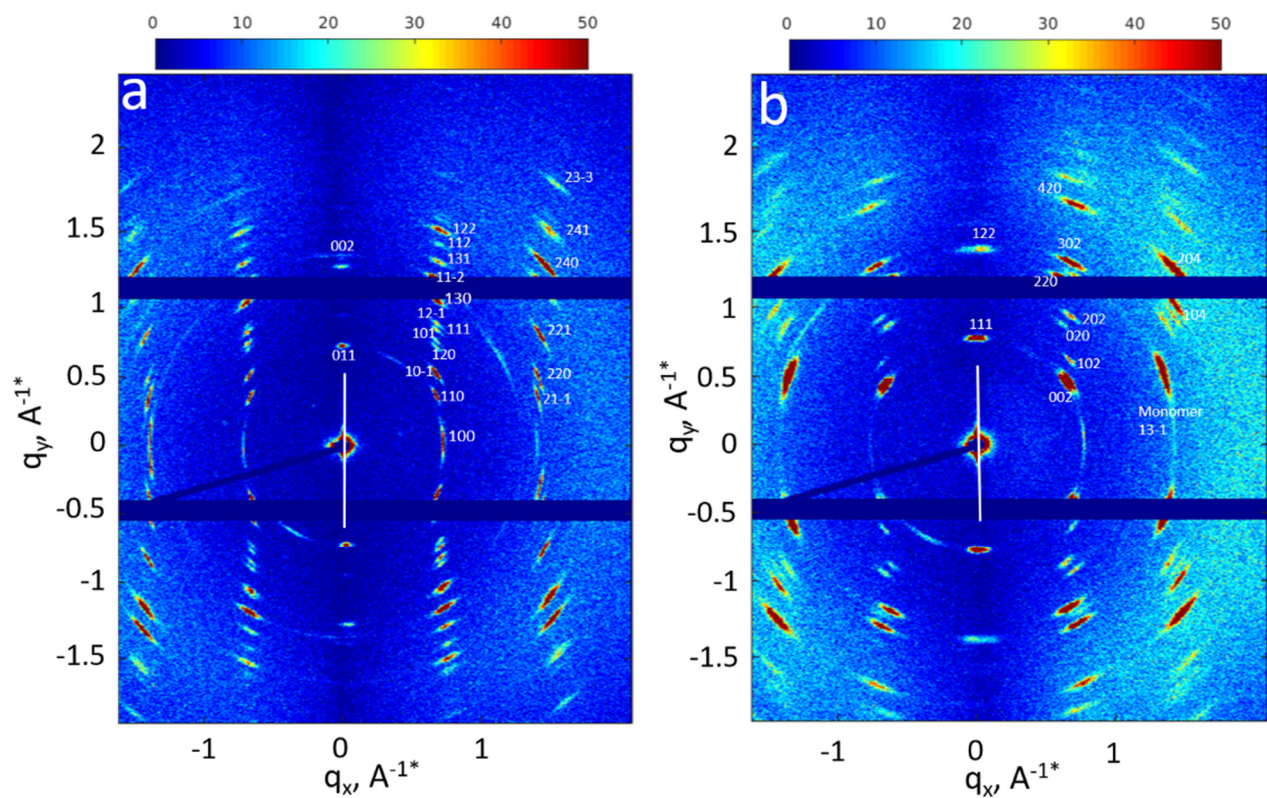


**Figure S13.** GIWAXS patterns for the (a) **9TBAE** monomer- and (b) SSRD-filled AAO templates. The film plane is indicated by a white line. As the diffraction patterns have four-quadrant symmetry, only the diffraction spots in the upper right quadrant are indexed here.

### GIWAXS: Calculation of the Diffraction Spot Position

Here, we discuss how to predict the locations of each diffraction spot for 9TBAE for comparison with the experimental patterns. A right-handed Cartesian coordinate system is established with the z-axis parallel to the incident X-rays and the y axis as the sample rotation axis. Thus, the 2D detector is parallel to the x-y plane.  $\beta$  is defined as the angle between the incident X-rays and the AAO surface. When  $\beta = 0$ , the AAO sample plane is parallel to the y-z plane and the unit normal vector  $\mathbf{n}_0$  of the corresponding crystal plane is equal to  $[\sin(\sigma), \cos(\sigma)\cos(\Phi), \cos(\sigma)\sin(\Phi)]$ , where  $\sigma$  is the elevation angle and  $\Phi$  is the azimuthal angle.

In GIWAXS experiments, the sample is rotated around the y-axis by  $\beta$  degrees counterclockwise and the resultant normal for a given plane  $\mathbf{n}$  can be calculated using an active rotation convention:

$$\mathbf{R} = \text{rot}(z, \alpha) \times \text{rot}(y, \beta) \times \text{rot}(z, \gamma)$$

In this case,  $\alpha = 0, \gamma = 0, \beta = 2^\circ$

Therefore,

$$\mathbf{n} = \begin{bmatrix} \cos(2^\circ) & 0 & \sin(2^\circ) \\ 0 & 1 & 0 \\ -\sin(2^\circ) & 0 & \cos(2^\circ) \end{bmatrix} \mathbf{n}_0.$$

A diffraction spot can appear on the detector when Bragg's law is satisfied, i.e.  $\cos^{-1}(\mathbf{n} \cdot \mathbf{z}) = 90^\circ - \theta$ , with  $\theta$  as the angle between the crystal plane and incident X-rays. Solving for  $\mathbf{n}$  using the above equations and then taking its projection onto the x-y plane provides the expected position of the corresponding diffraction spot on the 2D detector.

**Table S3:** Orientation of 9TBAE monomer crystals with the real space [1 0 0] direction along the surface normal yields good agreement between calculated and measured positions of diffraction spots, expressed as angles away from the AAO film plane.

Reflection	Calculated angle (°)	Measured angle (°)
011	0.2	0.8
002	0.3	0.9
100	83.3/96.7	87.1**
110	61.8	62.4
10-1	51.8	52.9
120	43.7	44.6
101	41.9	42.4
111	39.2	39.9
12-1	37.6	38.1
130	32.8	32.7
11-2	29.2	31.3
131	29.0	27.9
112	25.6	26.5
122	23.9	23.8
21-1	75.4	75.2
220	71.2	69.7
221	61.4	60.7
240	48.4	48.9
241	41.2	44.3
23-3	36.0	38.7

\*\*The apparent location of the 100 diffraction spot nearly along the surface normal is thought to arise due to merging of the two spots on either side of the normal into a single broad diffraction arc

**Table S4:** Orientation of 9TBAE dimer crystals with the real space [0 1 -1] direction along the surface normal yields good agreement between calculated and measured positions of diffraction spots, expressed as angles away from the AAO film plane.

Reflection	Calculated angle (°)	Measured angle (°)
111	0.2	1.2
002	52.6	53.9
102	45.4	46.0
020	38.1	37.1
202	34.4	36.6
220	29.8	28.7
302	26.3	28.9
420	20.6	22.8
122	0.3	0.9
104	51.3	54.4
204	46.2	48.1

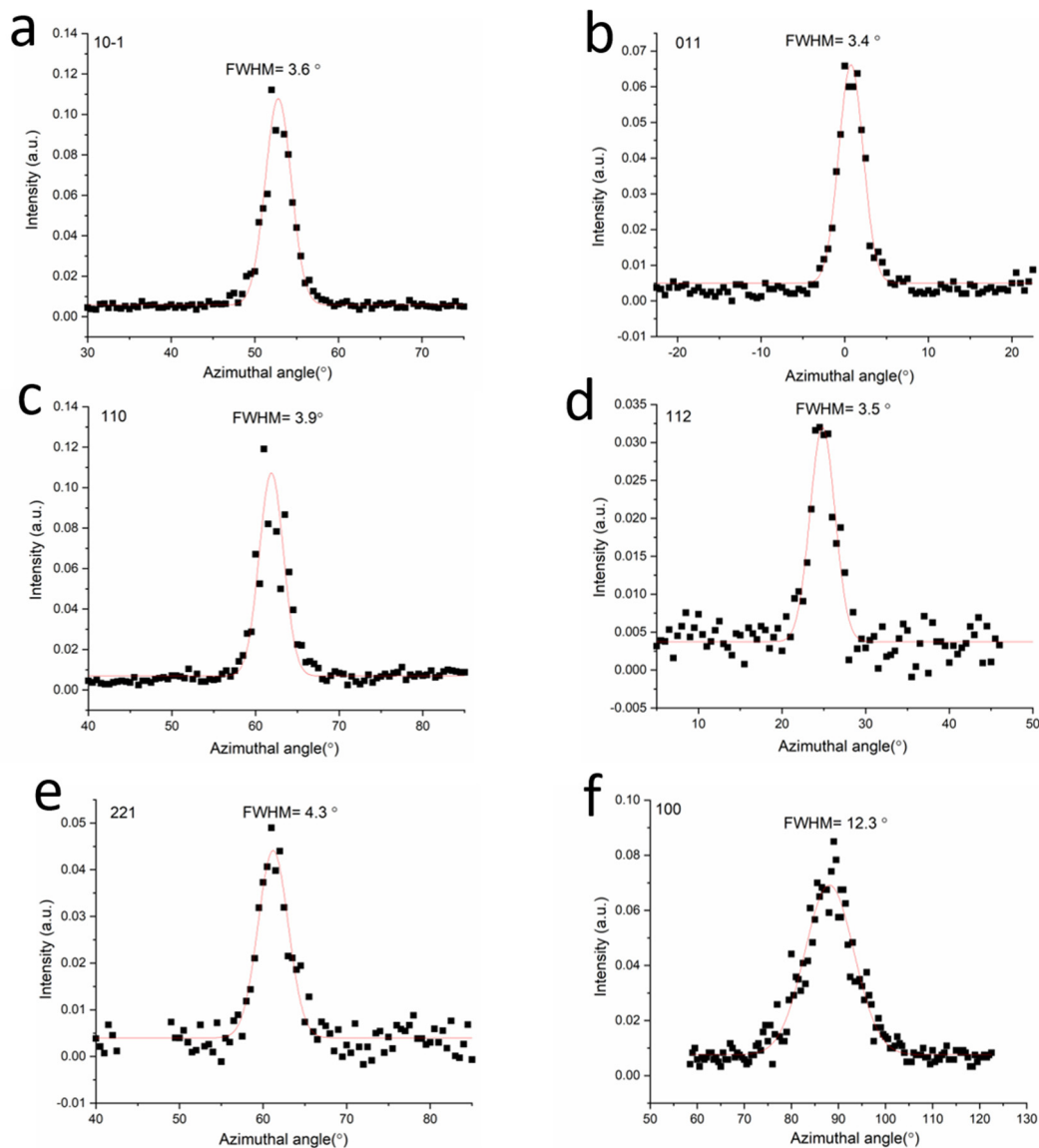


**Figure S14:** Azimuthal plots of the scattered X-ray intensity for several peaks within the pattern for 9TBAE monomer crystals. Directions along the film plane correspond to an azimuthal angle of 0/180°. FWHM values determined from Gaussian fits are listed for the (a) 10-1, (b) 011, (c) 110, (d) 112, (e) 221 and (f) 100 reflections. Compared to the other reflections (average FWHM= 3.7°), the 100 reflection has a substantially larger FWHM (12.3 °) suggesting that the two 100 diffraction spots have merged together into a single broad arc.

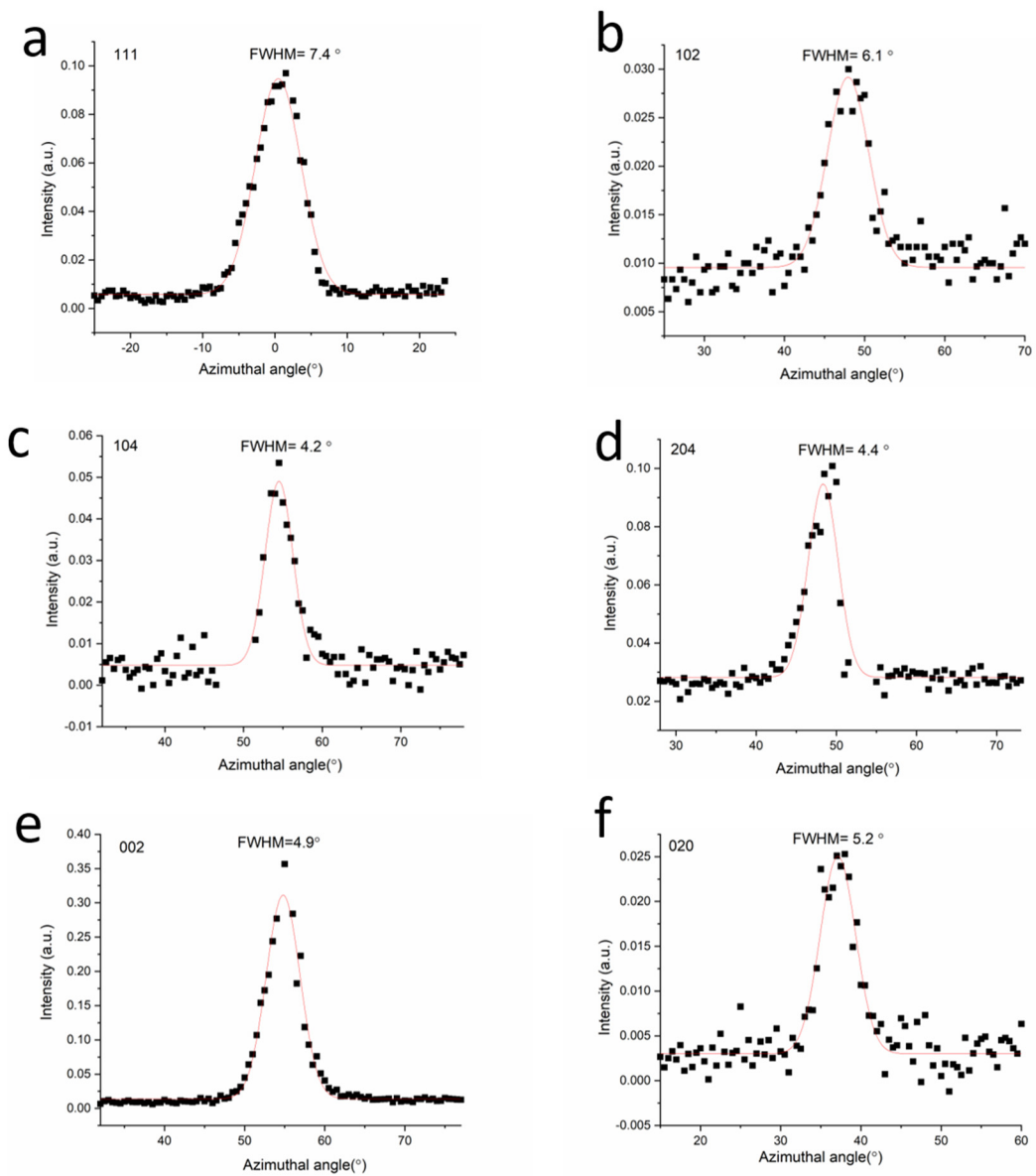
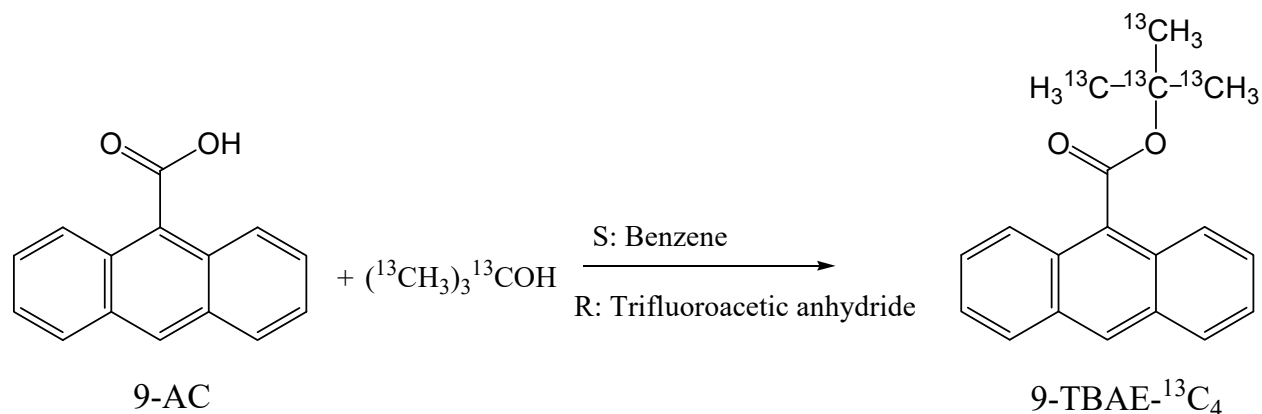


**Figure S15:** Azimuthal plots of the scattered X-ray intensity for several peaks within the pattern for **9TBAE** dimer crystals. Directions along the film plane correspond to an azimuthal angle of 0/180°. FWHM values determined from Gaussian fits are listed for the (a) 111, (b) 102, (c) 104, (d) 204, (e) 002 and (f) 020 reflections.

## Synthesis of New Molecules

### <sup>13</sup>C<sub>4</sub>-*t*Bu-9TBAE:

#### Overall Synthetic Route:



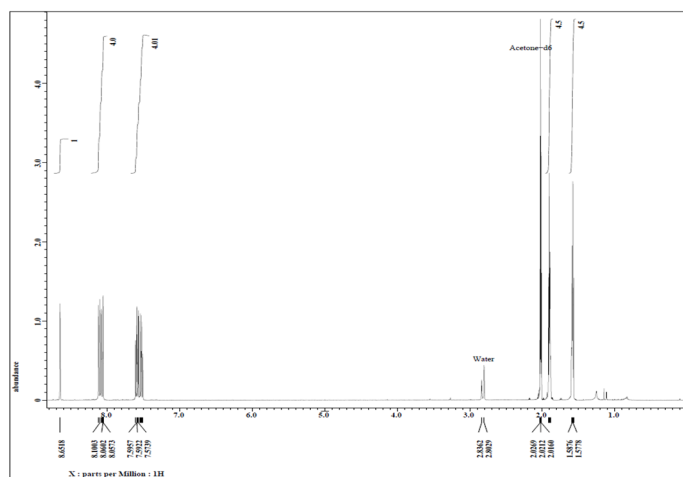
**Materials:** *tert*-Butanol-<sup>13</sup>C<sub>4</sub> (99 atom % <sup>13</sup>C, 98% (CP)) and 9-Anthracenecarboxylic acid (99%) were purchased from Sigma-Aldrich and used without further purification. Trifluoroacetic anhydride (99+%) was purchased from Acros Organics. Dry benzene was prepared by distilling reagent grade benzene over sodium and storing it over activated molecular sieves (3 Å).

**Instruments:** Melting point, uncorrected, was collected using Stuart melting point apparatus SMP3. For <sup>1</sup>H-NMR and <sup>13</sup>C-NMR structural characterization of the products, we used a JEOL JNM ECS 400 spectrometer. Proton chemical shifts were reported in ppm (δ) (Acetone-d<sub>6</sub>, δ 2.05 ppm with HOD and HOH at 2.77 and 2.83 respectively) and *J* values were reported in Hz. Carbon-13 chemical shifts were reported in ppm (δ) (Acetone-d<sub>6</sub>, δ = 29.8 q, 206 s). IR measurements were performed on an IR Affinity-1 FTIR from Shimadzu using a KBr disc.

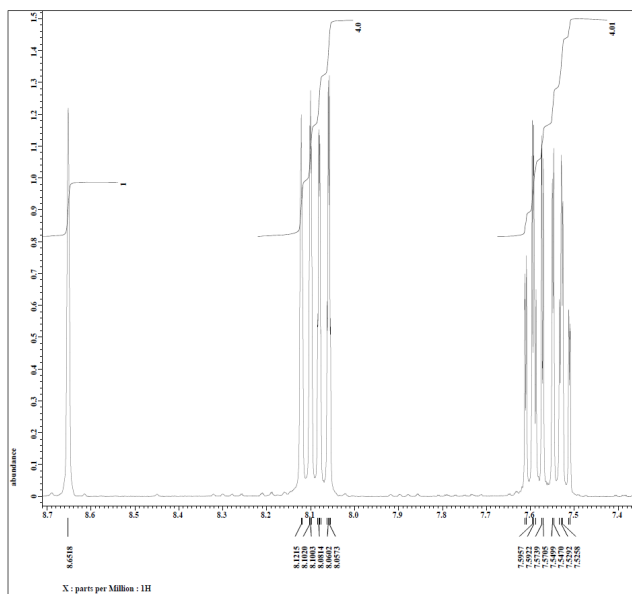
**Procedure:** Synthesis of the compound was performed according to the following scheme using a modified procedure for the synthesis of 9-TBAE.<sup>11</sup>

Into a flame-dried and Argon gas-purged 25 mL round bottom flask was added dry benzene (5mL) via syringe. Anthracene-9-carboxylic acid (0.22 g, 1 mmole) was added to the benzene to form a suspension. Trifluoroacetic anhydride (0.11 g, 0.076 mL, 1.1 mmoles, 1.1 Eq.) was added via syringe to the stirring suspension of 9-AC and allowed to stir at room temperature under a blanket of Argon gas for 20-30 minutes or until the 9-AC suspension went into solution. *tert*-Butanol-<sup>13</sup>C<sub>4</sub> (0.078 g, 0.095 mL, 1 mmole, 1 Eq. ) was added to the previous mixture and allowed to stir under argon for 16 hours. Reaction progress was monitored using TLC (silica gel, methylene dichloride). The organic phase was washed with aqueous NaHCO<sub>3</sub> to remove the unreacted 9-AC, trifluoroacetic acid and alcohol and then dried over anhydrous MgSO<sub>4</sub>. Additional 10 to 15 mL of dry benzene might be needed to compensate for the evaporated portions during workup. The organic phase was decanted and removed under reduced pressure to obtain crude product which was later recrystallized from minimum amount of boiling ethanol (10-15 mL) and water. Obtained light-yellow needles 0.17g (yield 60%).

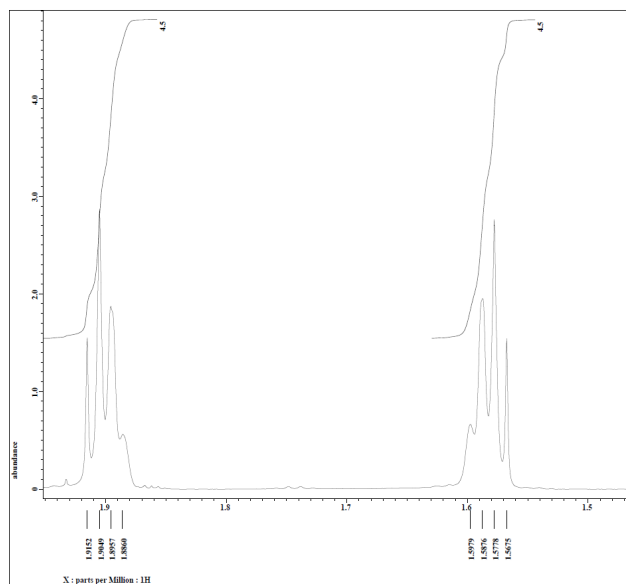
**Characterization:**  $^1\text{H NMR}$  (JEOL 400 MHz, Acetone- $d_6$ ):  $\delta = 1.56$ - $1.91$  (9H, ddd,  $J = 131, 7.8, 4.2$  Hz),  $7.52$ - $7.55$  (2H, m),  $7.57$ - $7.59$  (2H, m),  $8.06$ - $8.08$  (2H, d,  $J = 8$  Hz),  $8.10$ - $8.12$  (2H, d,  $J = 8$  Hz),  $8.65$  (1H, s).  $^{13}\text{C NMR}$  (JEOL 100 MHz, Acetone- $d_6$ ):  $\delta = 27.49$ - $27.89$  (d,  $(^{13}\text{C H}_3)_3$ - $^{13}\text{C}$ ,  $J = 40$  Hz),  $81.97$ - $83.15$  (q,  $(^{13}\text{C H}_3)_3$ - $^{13}\text{C}$ ,  $J = 40$  Hz),  $124.79$ ,  $125.63$ ,  $126.96$ ,  $127.75$ ,  $128.46$ ,  $128.69$ ,  $129.91$ ,  $131.16$ ,  $168.43$  (C=O). IR (KBr):  $\tilde{\nu} = 3051$  (w),  $2964$  (w),  $1712$  (C=O, s),  $1356$  (s),  $1237$  (s),  $1129$  (s),  $994$  (m)  $\text{cm}^{-1}$ . M.P. =  $155.8$ - $157.2$   $^\circ\text{C}$



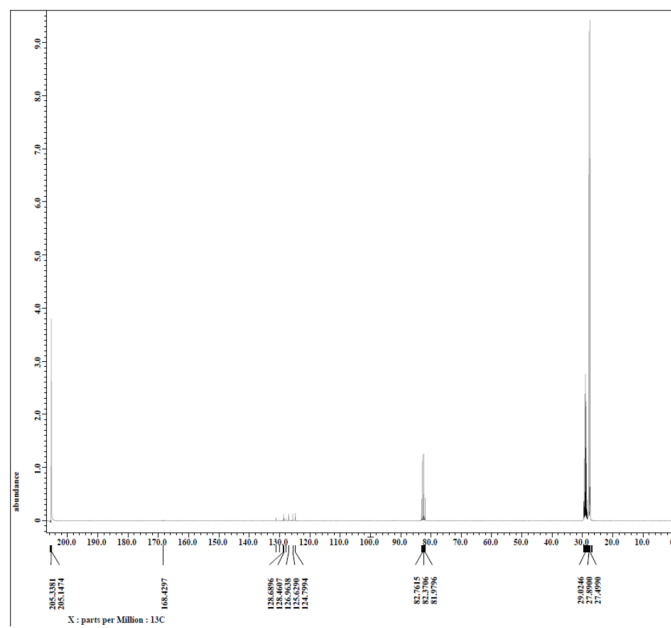
$^1\text{H NMR}$  of **9-TBAE- $^{13}\text{C}_4$**  in Acetone- $d_6$ .



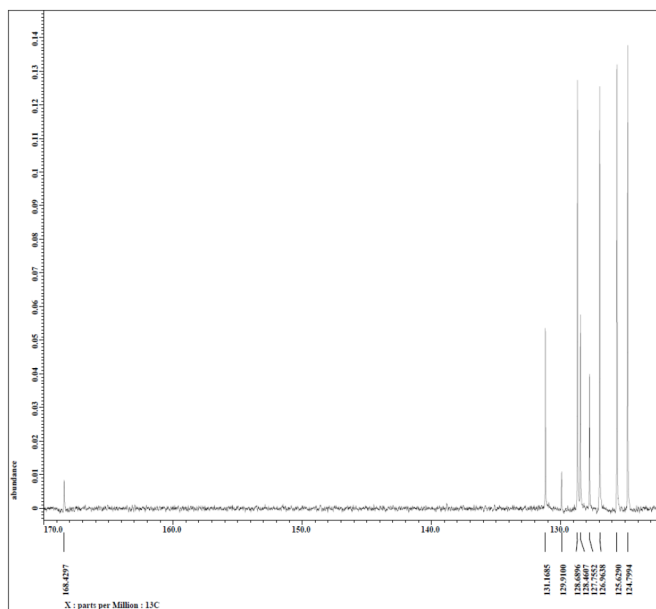
$^1\text{H NMR}$  of **9-TBAE- $^{13}\text{C}_4$**  in Acetone- $d_6$ , expanded aromatic region



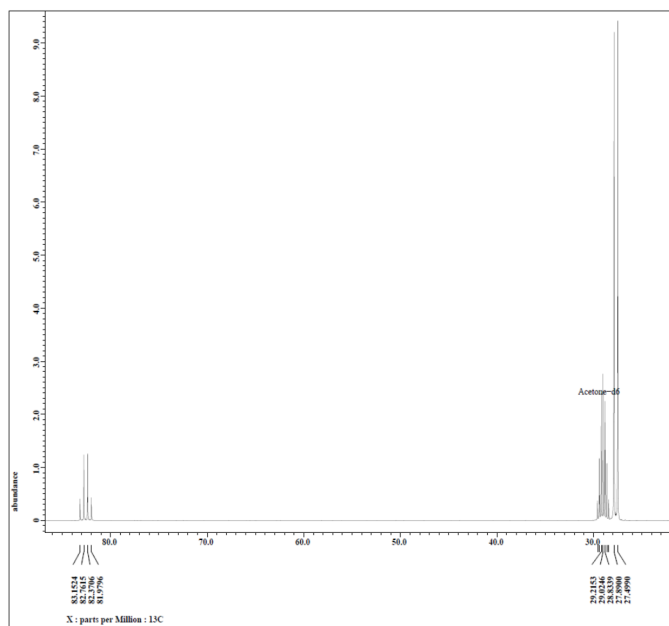
$^1\text{H}$ NMR of **9-TBAE- $^{13}\text{C}_4$**  in Acetone- $d_6$ , expanded aliphatic region.

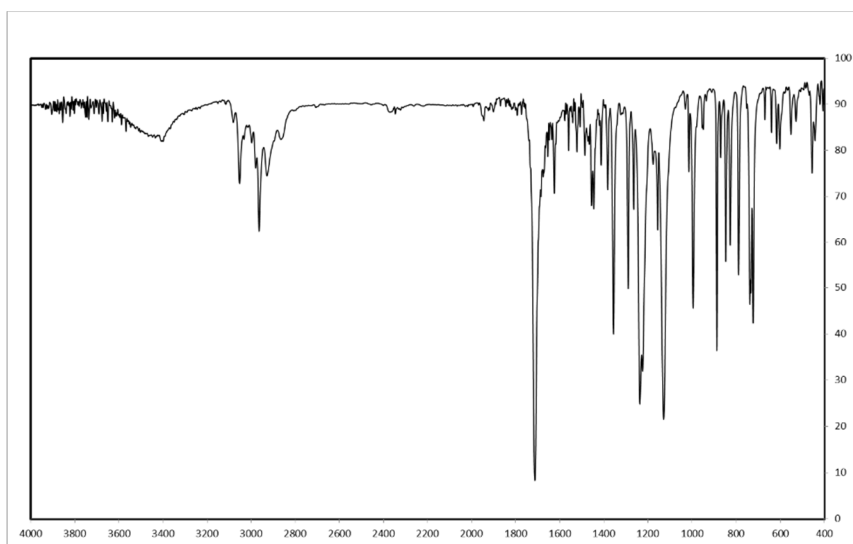


$^{13}\text{C}$ NMR of **9-TBAE- $^{13}\text{C}_4$**  in Acetone- $d_6$



$^{13}\text{C}$ NMR of **9-TBAE- $^{13}\text{C}_4$**  in Acetone- $\text{d}_6$  expanded Aromatic region

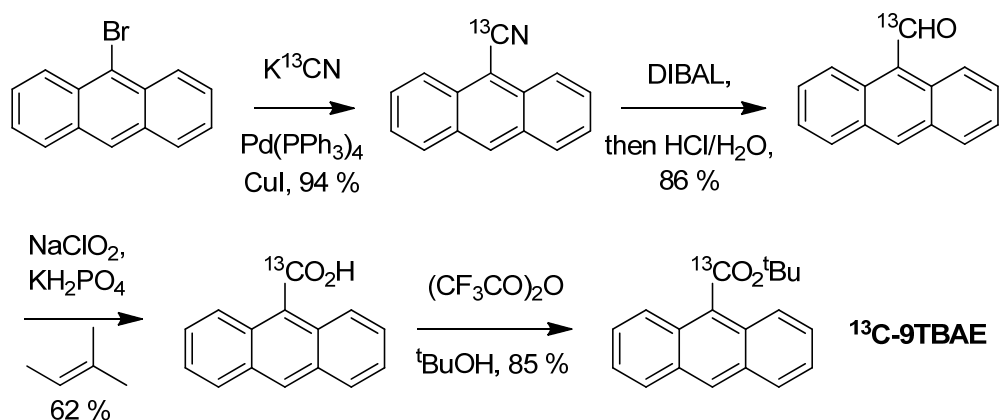




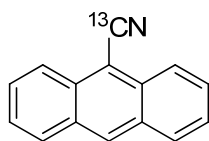
IR spectrum of **9-TBAE-<sup>13</sup>C<sub>4</sub>** mixed with KBr and pressed into a pellet.

### <sup>13</sup>C15-9TBAE:

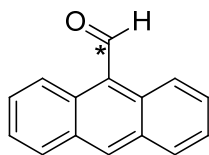
#### Overall Synthetic Route:



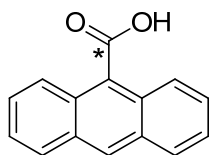
#### Synthetic Procedures and Characterization:



**9-anthracenecarbonitrile-<sup>13</sup>C9:** <sup>13</sup>C-enriched potassium cyanide (640 mg, 2 eq.) was pulverized via mortar and pestle, then added to a two-neck round-bottom flask containing 9-bromoanthracene (1.0 g, 1 eq.), copper (I) iodide (80 mg, 0.1 eq.), and tetrakis(triphenylphosphine)palladium(0) (240 mg, 0.05 eq.). The flask was sealed, purged with nitrogen, then filled with 25 mL of dry acetonitrile. The resulting solution was refluxed for 16 hours with magnetic stirring. The reaction was cooled, diluted with ethyl acetate, filtered through celite, washed with water and brine, then purified by silica gel column chromatography to yield **9-anthracenecarbonitrile-<sup>13</sup>C9** as a bright yellow solid (752 mg, 94% yield). <sup>1</sup>H NMR (400 MHz, CDCl<sub>3</sub>) δ 8.69 (s, 1H), 8.44 (d, *J* = 8.7 Hz, 2H), 8.09 (d, *J* = 8.5 Hz, 2H), 7.73 (t, *J* = 7.3 Hz, 2H), 7.60 (t, *J* = 7.7 Hz, 2H). <sup>13</sup>C NMR (100 MHz, CDCl<sub>3</sub>) δ 133.5, 132.9, 131.9, 131.8, 129.1, 126.5, 125.5, 121.2, 117.4 (<sup>13</sup>CN). MS (ESI) *m/z* calcd for C<sub>14</sub><sup>13</sup>C H<sub>10</sub>N (M+H)<sup>+</sup> 205.0847; found 205.0841.

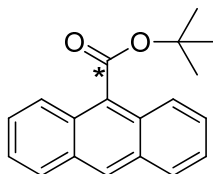


**9-anthraldehyde-<sup>13</sup>C9:** To a stirred solution of **9-anthracenecarbonitrile-<sup>13</sup>C9** (500 mg, 1 eq.) in dry toluene (10 mL), under nitrogen, was added diisobutylaluminum hydride (3.6 mL, 1M in heptane, 1.5 eq.). The reaction was heated to 80 °C for 1 hour, then cooled to 0 °C, at which point methanol (10 mL), water (5 mL), and HCl (12M, 1 drop) were added. The resulting biphasic solution was stirred vigorously at room temperature for 16 hours. The reaction contents were poured into water, extracted with ethyl acetate, washed with aqueous bicarbonate and brine, dried over MgSO<sub>4</sub>, and purified by silica gel column chromatography to yield **9-anthraldehyde-<sup>13</sup>C9** as a yellow solid (430 mg, 86% yield). <sup>1</sup>H NMR δ 11.54 (d, *J* = 173.9 Hz, 1H), 9.00 (d, *J* = 9.0 Hz, 2H), 8.72 (s, 1H), 8.08 (d, *J* = 8.4 Hz, 2H), 7.69 (t, *J* = 7.6 Hz, 2H), 7.56 (t, *J* = 7.8 Hz, 2H). <sup>13</sup>C NMR (100 MHz, CDCl<sub>3</sub>) δ 200.2, 193.2 (<sup>13</sup>CO), 161.6, 132.2, 129.5, 129.3, 128.7, 125.9, 123.7. MS (ESI) *m/z* calcd for C<sub>14</sub><sup>13</sup>C H<sub>10</sub>O (M<sup>+</sup>) 205.0765; found 207.0774.

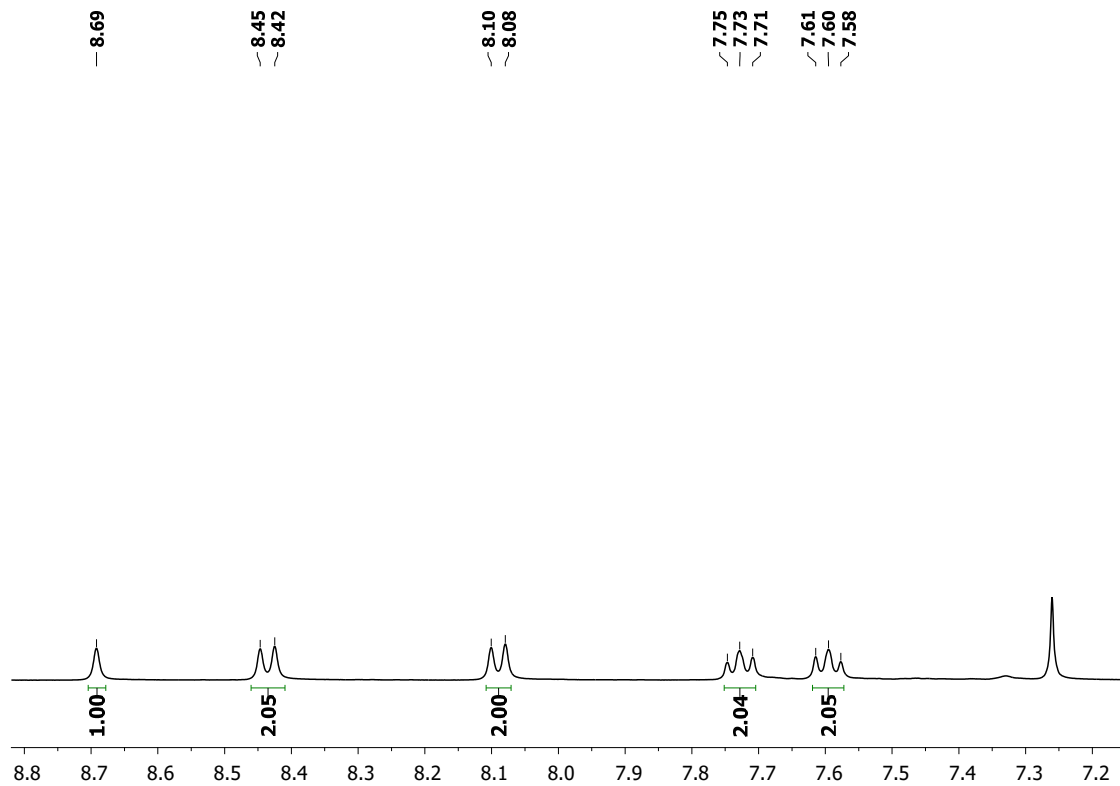


**9-anthroic acid-<sup>13</sup>C9:** To a stirred solution of **9-anthraldehyde-<sup>13</sup>C9** (414 mg, 1.0 eq.) in a mixture of THF:t-butanol:2-methyl-2-butene:water (30 mL, 3:3:3:1 ratio) was added monopotassium phosphate (544 mg, 2.0 eq.) and sodium chlorite (234 mg, 1.3 eq.) as concentrated aqueous solutions. The reaction was stirred vigorously for 6 hours at room temperature, then diluted into water, extracted with ethyl acetate, washed with mildly acidic water, and purified via silica gel column chromatography to yield **9-anthroic acid-<sup>13</sup>C9** as a yellow solid (276 mg, 62% yield). (400 MHz, CDCl<sub>3</sub>) δ 8.59 (s, 1H), 8.30 (d, *J* = 8.8 Hz, 2H), 8.05 (d, *J* = 8.4 Hz, 2H), 7.60

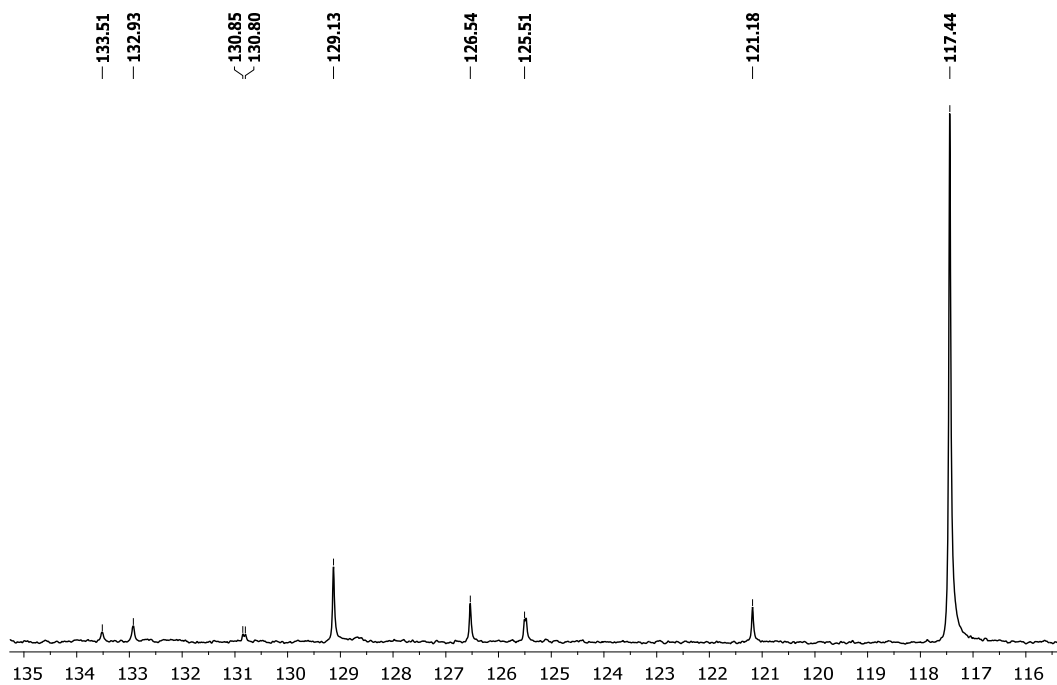
(t,  $J = 6.8$  Hz, 2H), 7.52 (t,  $J = 7.7$  Hz, 2H).  $^{13}\text{C}$  NMR (100 MHz,  $\text{CDCl}_3$ )  $\delta$  176.8, 176.4, 172.5 ( $^{13}\text{CO}_2\text{H}$ ), 131.1, 130.5, 128.9, 127.5, 125.7, 125.3. MS (ESI)  $m/z$  calcd for  $\text{C}_{14}^{13}\text{C}_9\text{H}_9\text{O}_2$  (M-H) $^+$ : 222.0636; found 222.0649.



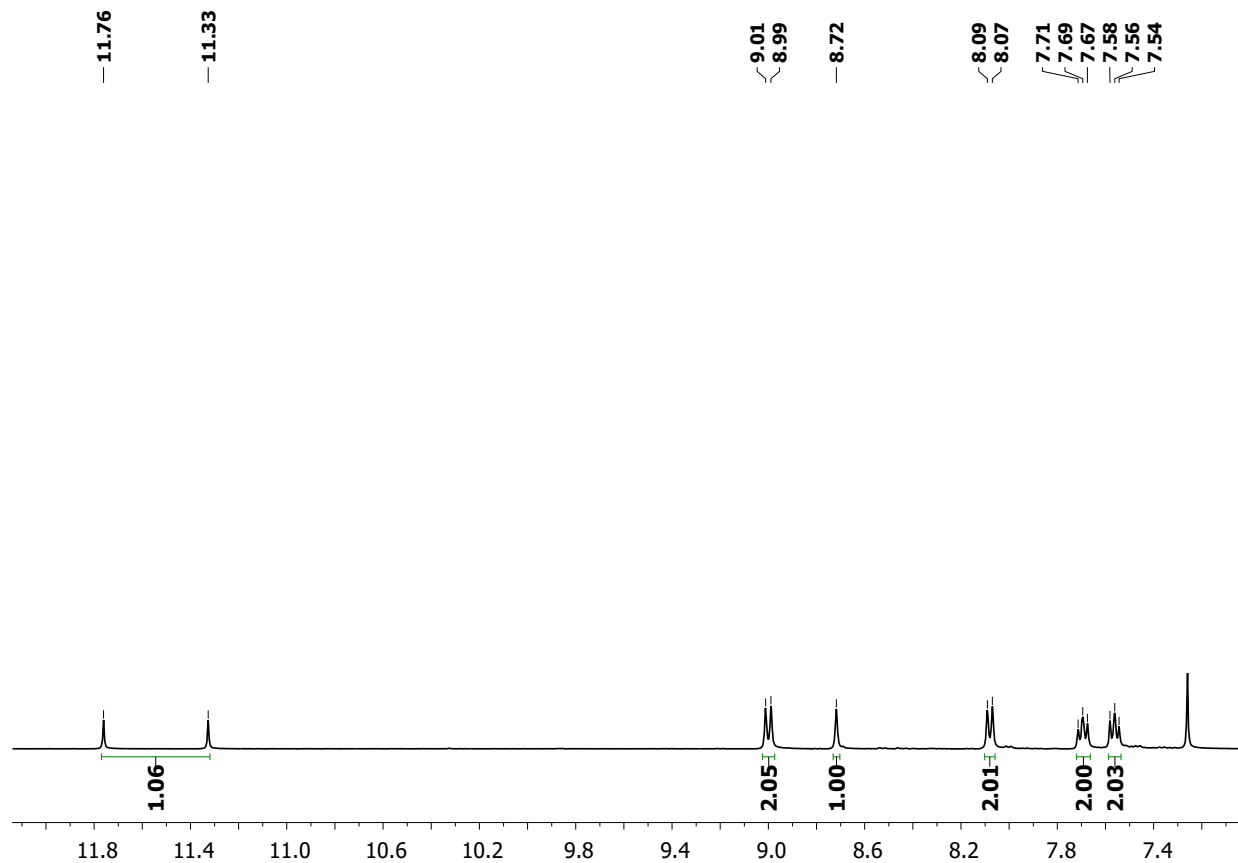
**9-anthroic acid *tert*-butyl ester- $^{13}\text{C}_9$ :** To a stirred solution of **9-anthroic acid- $^{13}\text{C}_9$**  (223 mg, 1.0 eq.) in dry toluene (15 mL), under nitrogen at 0 °C, was added trifluoroacetic anhydride (840 mg, 0.56 mL, 4.0 eq) dropwise. The reaction was heated to 25 °C for 30 minutes, then cooled to 0 °C. Anhydrous *t*-butanol (5 mL) was added, and the reaction was then stirred at room temperature for 18 hours. The reaction was diluted into ethyl acetate, washed several times with saturated sodium bicarbonate and water, dried with magnesium sulfate, and purified via silica gel column chromatography to yield **9-anthroic acid *tert*-butyl ester- $^{13}\text{C}_9$**  (237 mg, 85% yield) as a yellow solid.  $^1\text{H}$  NMR (400 MHz,  $\text{CDCl}_3$ )  $\delta$  8.51 (s, 1H), 8.10 (d,  $J = 8.6$  Hz, 2H), 8.04 (d,  $J = 8.3$  Hz, 2H), 7.56 (t,  $J = 6.8$  Hz, 2H), 7.50 (t,  $J = 6.9$  Hz, 2H), 1.81 (s, 9H).  $^{13}\text{C}$  NMR (100 MHz,  $\text{CDCl}_3$ )  $\delta$  171.2, 169.2 ( $^{13}\text{CO}_2\text{R}$ ), 164.1, 131.2, 128.7, 128.6, 126.8, 125.5, 125.0, 76.3, 28.6. MS (ESI)  $m/z$  calcd for  $\text{C}_{18}^{13}\text{C}_9\text{H}_{18}\text{O}_2$  (M) $^+$  279.1340; found 279.0929.



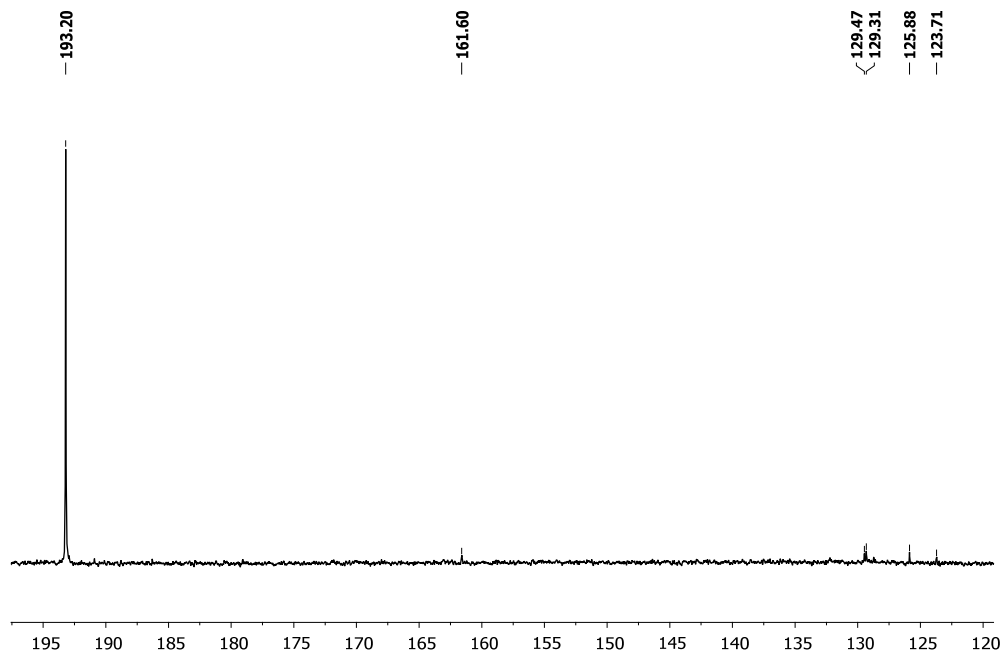
$^1\text{H}$  NMR spectrum of **9-anthracenecarbonitrile- $^{13}\text{C}9$** , 400 MHz,  $\text{CDCl}_3$ , 298K.



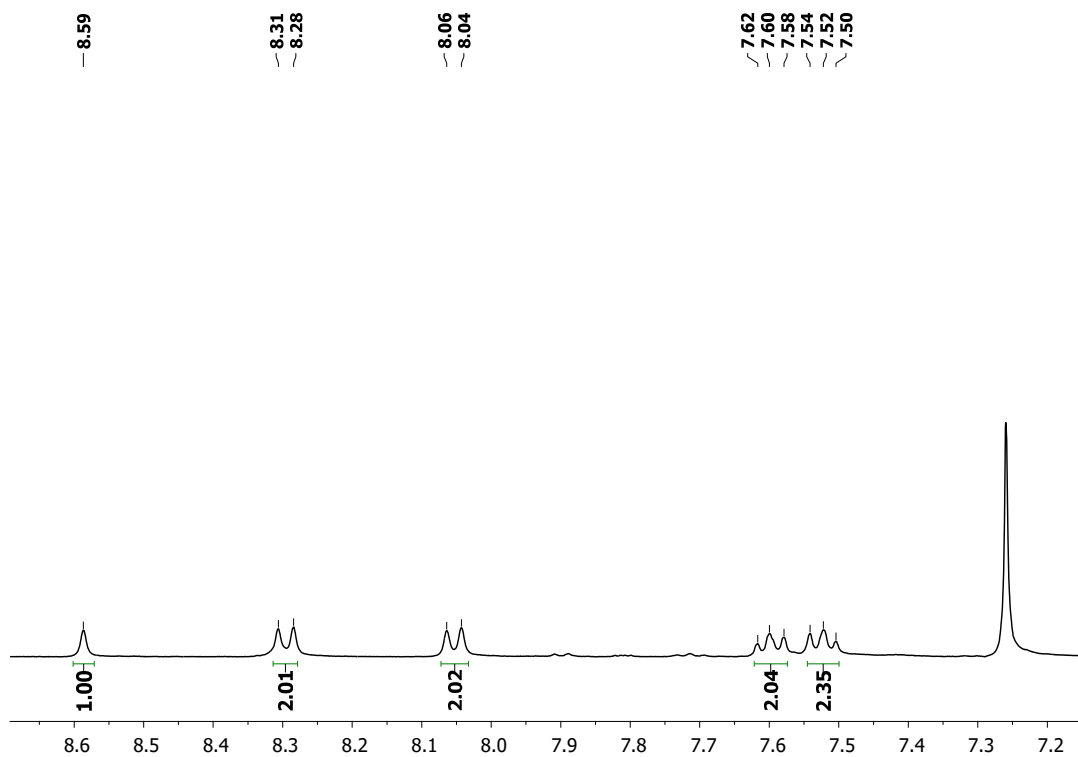
$^{13}\text{C}$  NMR spectrum of **9-anthracenecarbonitrile- $^{13}\text{C}9$** , 100 MHz,  $\text{CDCl}_3$ , 298K.



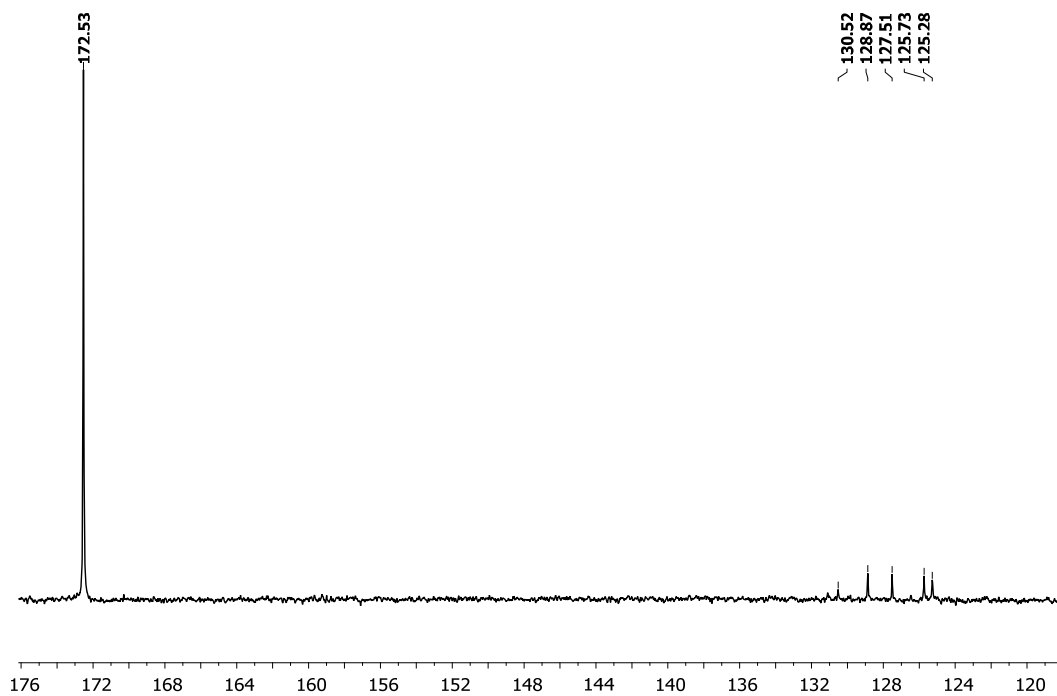
$^1\text{H}$  NMR spectrum of **9-anthraldehyde- $^{13}\text{C}_9$** , 400 MHz,  $\text{CDCl}_3$ , 298K.



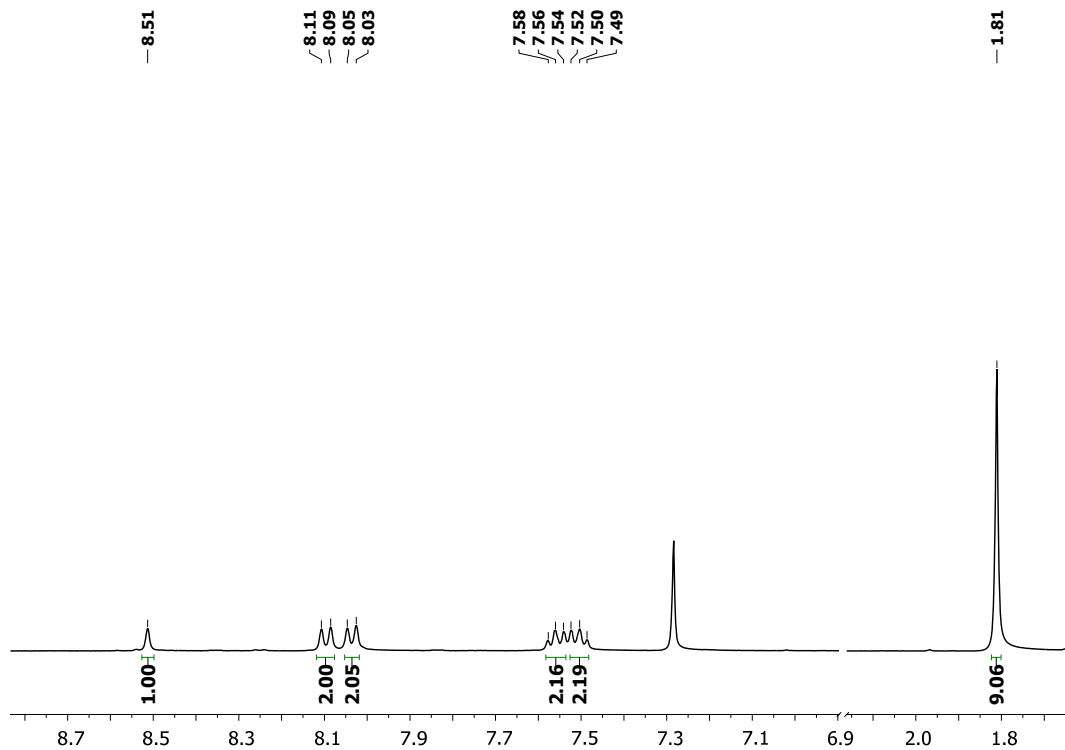
$^{13}\text{C}$  NMR spectrum of **9-anthraldehyde- $^{13}\text{C}_9$** , 100 MHz,  $\text{CDCl}_3$ , 298K.



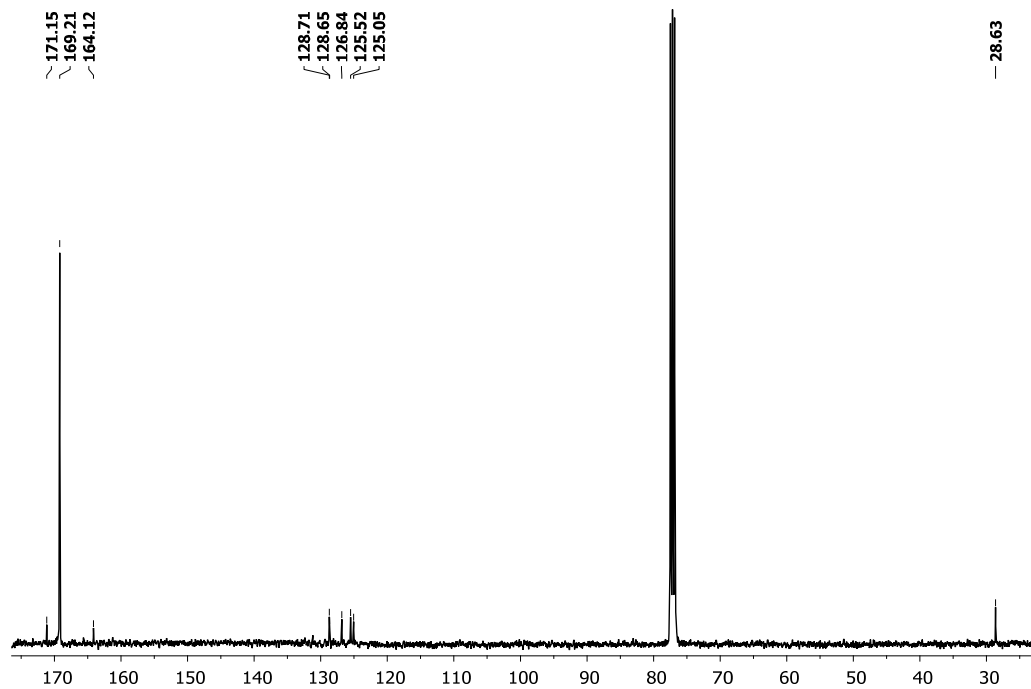
$^1\text{H}$  NMR spectrum of **9-anthroic acid- $^{13}\text{C}9$** , 400 MHz,  $\text{CDCl}_3$ , 298K.



$^{13}\text{C}$  NMR spectrum of **9-anthroic acid- $^{13}\text{C}9$** , 100 MHz,  $\text{CDCl}_3$ , 298K.



$^1\text{H}$  NMR spectrum of **9-anthroic acid *tert*-butyl ester- $^{13}\text{C}9$** , 400 MHz,  $\text{CDCl}_3$ , 298K.



$^{13}\text{C}$  NMR spectrum of **9-anthroic acid *tert*-butyl ester- $^{13}\text{C}9$** , 100 MHz,  $\text{CDCl}_3$ , 298K.

## References

1. Hartman, J. D.; Kudla, R. A.; Day, G. M.; Mueller, L. J.; Beran, G. J. O., Benchmark fragment-based <sup>1</sup>H, <sup>13</sup>C, <sup>15</sup>N and <sup>17</sup>O chemical shift predictions in molecular crystals. *Physical Chemistry Chemical Physics* **2016**, *18* (31), 21686-21709.
2. Yang, C.; Zhu, L.; Kudla, R. A.; Hartman, J. D.; Al-Kaysi, R. O.; Monaco, S.; Schatschneider, B.; Magalhaes, A.; Beran, G. J. O.; Bardeen, C. J.; Mueller, L. J., Crystal structure of the meta-stable intermediate in the photomechanical, crystal-to-crystal reaction of 9-tert-butyl anthracene ester. *Crystengcomm* **2016**, *18* (38), 7319-7329.
3. Hartman, J. D.; Monaco, S.; Schatschneider, B.; Beran, G. J. O., Fragment-based <sup>13</sup>C nuclear magnetic resonance chemical shift predictions in molecular crystals: An alternative to planewave methods. *The Journal of Chemical Physics* **2015**, *143* (10), 102809.
4. Young, R. P.; Lewis, C. R.; Yang, C.; Wang, L.; Harper, J. K.; Mueller, L. J., TensorView: A software tool for displaying NMR tensors. *Magn Reson Chem* **2019**, *57* (5), 211-223.
5. Kolbert, A. C.; Griffin, R. G., Two-dimensional resolution of isotropic and anisotropic chemical shifts in magic angle spinning NMR. *Chemical Physics Letters* **1990**, *166*, 87-91.
6. Hung, I.; Gan, Z. H., An efficient amplification pulse sequence for measuring chemical shift anisotropy under fast magic-angle spinning. *J Magn Reson* **2011**, *213* (1), 196-199.
7. Morcombe, C. R.; Zilm, K. W., Chemical shift referencing in MAS solid state NMR. *J Magn Reson* **2003**, *162* (2), 479-486.
8. Herzfeld, J.; Berger, A. E., Sideband intensities in NMR spectra of samples spinning at the magic angle. *The Journal of Chemical Physics* **1980**, *73*, 6021-6030.
9. Mueller, L. J., Tensors and Rotations in NMR. *Concept Magn Reson A* **2011**, *38A* (5), 221-235.
10. Macrae, C. F.; Edgington, P. R.; McCabe, P.; Pidcock, E.; Shields, G. P.; Taylor, R.; Towler, M.; van De Streek, J., Mercury: visualization and analysis of crystal structures. *J Appl Crystallogr* **2006**, *39*, 453-457.
11. Al-Kaysi, R. O.; Muller, A. M.; Bardeen, C. J., Photochemically driven shape changes of crystalline organic nanorods. *J. Am. Chem. Soc.* **2006**, *128*, 15938-15939.